Heliyon 10 (2024) e38087

Contents lists available at ScienceDirect

Heliyon

journal homepage: www.cell.com/heliyon

Research article

Performance analysis, statistical modeling, and multiple response optimization of a novel fixed-bed quartz reactor packed with Ba-Pt@γ-AL_2O_3 using response surface methodology

Javad Sajedifar, Seyyed Bagher Mortazavi *, Hasan Asilian Mahabadi

Department of Occupational Health and Safety Engineering, Faculty of Medical Sciences, Tarbiat Modares University, Tehran, Iran

ARTICLE INFO

Keywords:
Response surface methodology
Optimization
NO_X storage reduction
Reactor
Preheating chamber

ABSTRACT

In the present study, a novel fixed-bed continuous reactor with a preheating chamber was designed to be utilized for the practical application of removal studies of dangerous pollutants, especially NO_X removal by NO_X Storage Reduction (NSR) catalysts on a laboratory scale. The reactor's design and operational parameters, including outer wall temperature (50–600 °C), volumetric flow rate (0.3–3 L/min), wall temperature time (0.16–10 min), and granule surface area inside the preheating chamber (0–270 cm^2), were statistically modeled and optimized using Response Surface Methodology (RSM). For more logical and effective parameter optimization, the ratio of gas and catalyst temperatures and pressure drop to the reactor outer wall temperature (GT/ROWT, CT/ROWT, and PD/ROWT) were also included in the optimization process. Experimental results showed that gas temperature, catalyst temperature, and pressure drop ranged from 31 to 177 °C, 51–585 °C, and 7–153 Pa, respectively. Optimal conditions were determined to be an outer wall temperature of 230 °C, a volumetric flow rate of 3 L/min, a wall temperature time of 0.16 min, and a granule surface area of 67.3 cm^2. The results demonstrated that outer wall temperature, flow rate, time, and surface area of granules have significant and interaction effects on the responses and should be considered when researchers assess the removal efficiency of thermal catalysts.

1. Introduction

Air pollution, especially in urban areas, is an essential historical concern related to combustion processes. Meanwhile, mobile sources significantly contribute to the production of air pollution. Based on data provided in South Korea, mobile pollutant sources, including road and non-road vehicles, are the most prominent emission sources of nitrogen oxides (NOx). Cars are the primary source of NOx pollution on roads [1]. NOx emissions from mobile sources account for approximately half of all NOx produced, resulting in strict regulations for vehicle emissions [2]. Emitting NOx is an important environmental issue and can severely affect human health [3]. Exposure to high levels of NOx causes eye and skin irritation and respiratory damage [4]. Besides, from an environmental point of view, nitrogen oxides contribute to the formation of acid rain in the presence of sunlight [5], which is an important environmental

* Corresponding author. Department of Occupational Health and Safety Engineering, Faculty of Medical Sciences, Tarbiat Modares University, P. O. Box: 331-14115, Tehran, Iran.

E-mail addresses: javad.sajedifar@modares.ac.ir (J. Sajedifar), mortazav@modares.ac.ir (S.B. Mortazavi), Asilia_h@modares.ac.ir (H. Asilian Mahabadi).

https://doi.org/10.1016/j.heliyon.2024.e38087
Received 3 June 2024; Received in revised form 14 September 2024; Accepted 17 September 2024
Available online 18 September 2024

concern. In addition, NOx contribute to producing photochemical smog and ground-level ozone [6,7]. Therefore, effective mitigation strategies are essential to address these impacts and improve both air quality and ecosystem health. According to the opinion of the vast majority of air pollution experts, controlling pollutants, especially air pollutants from the source, is one of the appropriate solutions. In this regard, one of the most appropriate methods of controlling the pollutants emitted from the exhaust of cars is using catalytic converters. Using heterogeneous catalysts is one of the most important and influential ways to reduce the effects of nitrogen dioxide in the environment [8]. So far, heterogeneous catalytic processes have been the most efficient solutions for environmental problems due to their high efficiency and selectivity towards removing undesirable by-products, such as atmospheric pollutants from vehicle exhaust gases [9]. When it comes to comparison, lean burn gasoline direct injection (GDI) engines can provide significant fuel savings and fewer CO_2 emissions over port-injected engines (PFI) (working with a stoichiometric air-to-fuel ratio (≈14.7:1)). Although the presence of excess air in GDI engines prevents the production of high concentrations of nitrogen oxides (NOx), it renders standard three-way catalysts (TWC) ineffective for NOx removal [2,10]. A potential solution to this problem is using a Lean NOx Trap (LNT) or NO_X Storage Reduction (NSR) [11–14], which typically consists of a catalyst comprising one or more precious metals and an alkali metal oxide or alkaline earth metal placed over a high specific surface such as alumina. NSR can absorb NOx from the exhaust gas and store it under lean conditions, and then release and convert it to nitrogen by changing the engine operation to the stoichiometric mode or rich mode ($\lambda < 1$) [15]. The NSR catalyst is particularly suitable for automotive applications due to its high efficiency in reducing NOx emissions under lean-burn conditions. NSR catalysts are compatible with stringent emission standards, making them essential for meeting environmental regulations. Their ability to adapt to different driving conditions, such as city and highway environments, further enhances their suitability for automotive use [16,17]. It should be noted that a large amount of research in the field of catalysts, especially NOx Storage Reduction (NSR) catalysts, has been conducted using fixed-bed reactors with small quantities of catalysts in universities and research centers. For instance, Bonzi et al. conducted a comprehensive analysis of the catalytic behavior during the NO_X storage-reduction process in single Ba-Pt @Al_2O_3 LNT, FeZSM-5 SCR systems, and the combined LNT + SCR system under clean conditions (without CO_2 and H_2O). The study revealed that when the SCR catalyst is positioned downstream of the NSR catalyst bed, the ammonia released from the LNT catalyst during the rich phase is stored in the downstream SCR catalyst and converted to N_2 during the lean phase. This configuration enhances both NO_X removal efficiency and N_2 selectivity [18]. Moreover, Cao Lijuan et al. investigated the effect of CO_2 concentration and inlet flow temperature on absorption pathways in NO_X combustion under lean conditions (82). To examine this effect, they developed a new LNT absorption model based on CHEMKIN SOFT. They believed that the model considers both nitrate and nitrite absorption pathways [19].

A catalytic fixed-bed reactor is a cylindrical tube containing active elements like particles, open foams, or structured inserts. The particles may be spheres, cylinders, or rings. However, more complex shapes such as wagon wheels, multiple lobes, multichannel cylinders, and cylinders with external flutes or grooves have been used in specific processes [20]. Fixed-bed reactors come in all sizes; however, researchers generally group them as laboratory-scale, pilot plant-scale, or commercial-scale. Laboratory-scale fixed-bed reactors are operated to create a new process, analyze a new solid-supported catalyst, certify a different catalyst for commercial use, and maintain an existing commercial process [21]. Chemical reactors are developed to make the chemical process as efficient as possible. Controlling temperature, mixing, and tracking processes are frequently necessary for process optimization and control. In such cases, the reactor includes a heating/cooling jacket, an inner heater, a stirrer, and ports for collecting samples or attaching probes. The chemical reactor needs to be able to adjust in accordance with the changes of the reaction system [22]. According to the definition provided, a reactor with a diameter of less than 1 mm is called a microreactor; if its diameter is between 1 mm and 1 cm, it is called a mesoreactor [23]. The transport phenomena (heat and mass transfer and flow field) and reaction kinetics interact and impact each other simultaneously during the reactor operations. Often, chemical reactions are highly endothermic or exothermic. The heat generated or consumed influences the temperature of the flow field and particles, and most transport parameters also rely on temperature. The flow patterns have a significant effect on the temperature distribution in the reactor. In order to make an exact model of fixed beds, all these variations and interactions must be considered [20]. Heat transfer is crucial in studying various catalytic processes, such as removing hazardous pollutants. The laboratory-scale reactors are placed inside a furnace chamber with a heated section. They are heated by a furnace chamber that may be configured vertically or horizontally on the laboratory setup [24]. As a result, several studies (e.g. Ref. [25]) have explored these issues. In packings of mono- and polydispersed spheres, Yang et al. [26] investigated the impact of the fixed bed geometrical features (such as particle size and wall distance) on flow and temperature profile. The authors demonstrated that when uniform spheres are packed with a fixed heat flux at the wall, the velocity profile is greater and the temperature is lower close to the wall due to significant voidage. They found that the voidage near the wall was reduced when polydispersed particles were packed with smaller particles close to the wall, which improved the temperature gradient caused by wall effects. Because of the smaller particles, this approach improved the efficiency of radial heat transmission, but the pressure drop was higher. Comparable research was done by Zhang et al. [27] for beds of uniformly distributed cylindrical particles, and they found that the flow and temperature gradients along the wall were quite comparable to those seen in the packing of spheres.

An undergraduate course on reaction kinetics and reactor design must include experiments using tubular reactors. However, for such experiments to be successfully designed, several requirements relating to safety, simplicity of design and analytical needs, acceptable cost, and educational value must be met [28]. The data collected appropriately must reflect steady-state chemical activity and selectivity, regardless of whether laboratory research of heterogeneous catalysis are focused on developing kinetic models of the reaction system or assessing catalysts. The effects of interphase and intraparticle heat and mass diffusion, as well as both axial and radial nonuniformities in the temperature profiles of the gas and catalyst phases, tend to skew the data and make further studies challenging. Refrain from considering diffusional effects, reaction rate data might provide misleading rate expressions. The plant reactor might run at devastating levels of activity and yield with scale-up based on the presumption that laboratory statistics solely represent chemical events. A catalyst evaluation based on such information may result in the best catalyst being rejected and a

somewhat subpar contender being chosen for commercial usage. Considerable attention must be given to the non-chemical aspects of reactor behavior [29]. Lab-scale tubular reactors are widely used for catalyst evaluation due to their high efficiency and relatively low cost compared to industrial-scale reactors. However, a key challenge in optimizing reactor performance—measured in terms of conversion, yield, or selectivity—is the precise control of operational parameters such as temperature and pressure drop within the reactor. One of the significant technical limitations in current reactor designs is the difficulty in accurately measuring the temperature at various points within the reactor, particularly the gas and catalyst temperature as well as the pressure drop. Higher reactor performance requires precise control of operational factors such as the gas and catalyst temperature and the pressure drop. Several operational and technical limitations hinder the detection of the temperature at different points in the reactor (before, inside, and after the catalyst). For example, Sudden and gradual temperature increases can cause critical damage to the quartz reactor wall due to the different expansion coefficients between the metal thermocouples and quartz. Additionally, filling and emptying a reactor (with an in-situ thermocouple or a thermowell [30]) is time-consuming and may also cause physical damage to the thermocouple and preformed catalyst granules while loading the catalyst inside the reactor. Therefore, it is essential to detect the temperature outside the reactor (on the reactor wall at a certain point) and statistically model the temperature inside the reactor. This method could extend the life of the reactor and catalyst granules and enable easy evaluation of the catalyst and gas temperature as the most influential factors in determining the catalyst performance for the removal of pollution. In light of discussion above and due to the lower cost and more control of the influencing parameters, much research has been conducted on a laboratory scale using small reactors. However, in many thermal catalyst studies, the investigated temperature in the studies faces challenges. Various research studies have employed different temperature parameters, including reactor outer wall temperature, gas temperature before and after the catalyst, and catalyst temperature. These temperature variations can significantly affect the removal efficiency of the evaluated catalyst. In the present study, we designed and built a fixed-bed continuous reactor with a pre-heating chamber to remove nitrogen monoxide and other dangerous pollutants from the air. With the construction of this new reactor and the optimization of integrated design-operational parameters, future studies can carry out, simulate, and optimize removal reactions of nitrogen monoxide and other gaseous pollutants emitted from car exhausts, chimneys of power plants, and other industrial units on a laboratory scale with high accuracy and precision, utilizing various catalysts. The design improvements suggested in this study should simplify the experiment, enhance result reproducibility, and expedite data collection within the time constraints.

2. Materials and methods

2.1. Reactor design with preheating chamber

According to the published research in this field [31–33] and available facilities, a continuous flow reactor made of quartz (high thermal resistance up to about 1200 °C) with an internal diameter of 8 mm and an external diameter of 10 mm with a total length of 36 cm and with a preheating chamber (length of the initial part of the reactor = 10 cm, preheating chamber = 8 cm and the end part of the reactor = 18 cm) was designed and used for various tests of thermal catalysts in the present research. The coned inlet section of the preheating chamber reduced the distortion of flow distribution to the packing quartz granules [34]. The preheating chamber was considered for maximum air contact with the granules inside the chamber. The granular materials were added gradually to the preheating chamber to ensure a normal distribution and prevent bridging. The granules used in the preheating chamber were neutral quartz granules. The quartz granules with smooth surfaces were mostly spherical or close to it. In order to prevent the displacement and exit of these granules, a 316 stainless steel net with a wire diameter of 0.4 mm and 20 mesh was placed at the end of the preheating chamber. The granules used in the preheating chamber (ID = 21 mm, ED = 23 mm) have an average diameter of 2.4 mm and an average weight of 0.01706 g (by randomly measuring the diameter and weight of 11 granules; each measurement was repeated five times), according to which other physical characteristics include: surface area, volume, bulk density and surface density, as well as the required weight of the quartz granules was calculated to control different levels of surface area variable (Table 1). All length and weight measurements were measured using a TUFF caliper with an accuracy of 0.1 mm and a Sartorius BP210D digital scale with an accuracy of 0.01 mg. Argon, grade 5 (99/999 purity), was used as a carrier gas and 1gr of Ba-Pt@γ-AL_2O_3 catalyst with a mesh of 30–50

Table 1
Physical characteristics of quartz granules.

Number	Diameter (mm)	Weight (gr)	Surface area (mm^2)	Volume (mm^3)	Volume density (gr/cm^3)	Surface density (gr/cm^2)
1	2.3	0.016	16.61	6.367	2.583	0.099
2	2.3	0.015	16.61	6.367	2.417	0.092
3	2.3	0.015	16.61	6.367	2.368	0.09
4	2.6	0.019	21.226	9.198	2.173	0.094
5	2.4	0.016	18.086	7.234	2.324	0.092
6	2.5	0.018	19.625	8.177	2.322	0.096
7	2.4	0.016	18.086	7.234	2.228	0.089
8	2.55	0.019	20.417	8.677	2.272	0.096
9	2.6	0.021	21.226	9.198	2.315	0.1
10	2.1	0.011	13.847	4.846	2.319	0.081
11	2.4	0.016	18.086	7.234	2.295	0.091
Mean	2.404	0.017	18.221	7.275	2.345	0.093
SD	0.145	0.002	2.17	1.296	0.101	0.005

(height of catalyst bed = 33 mm and ID of reactor = 8 mm; catalyst volume = 1.66 ml) fixed from above and below by 100 mg of dense glass wool (thickness = 6 mm and D = 8 mm) placed in the reactor in all tests. The schematic of the quartz reactor with the preheating chamber is given in Fig. 1. The insulating flange, consisting of aluminum veneer and stone wool, was installed at the top and bottom of the electric furnace. Its purpose was to prevent heat loss and ensure a uniform temperature distribution throughout the reactor. This was achieved by minimizing heat transfer to the exterior regions of the electrical furnace. The effectiveness of this insulation method was confirmed by temperature measurements along the outer wall of the reactor axially, which showed a uniform reactor wall temperature.

2.2. Synthesize the catalyst of Ba-Pt @γAL_2O_3

Due to the affinity of the γ-Al_2O_3 surface for metal catalysts and its thermal stability, crystalline γ-Al_2O_3 is often used as a base and support material for catalysts, showing a relatively high specific surface area. In line with the development of high-performance NSR (NOx Storage Reduction) catalysts, γ-Al_2O_3 has been used as one of the most important supports in catalysts [35]. The γ-alumina base is obtained by calcination at 700 °C from a commercial alumina material. In this study, a Ba-Pt@γ-Al_2O_3 (1/20/100, w/w) catalyst was used. This catalyst was prepared by wet impregnation of a commercial alumina sample with platinum dinitro diamine aqueous solution (5 % Pt in ammonium hydroxide) and subsequently with barium acetate solution (Aldrich, 99 %). In this way, Ba-Pt@γ-Al_2O_3 was prepared by incipient wet impregnation of a Pt@γ-Al_2O_3 (1/100 w/w) sample (which itself is prepared by incipient wet impregnation of γ-Al_2O_3 by platinum dinitro-diamine aqueous solution) by barium acetate. After each peregnation step, the catalyst powder and sample were air-dried overnight at 80 °C and calcined at 500 °C for 5 h (heating and cooling rate = 1 °C/min), pressed at 150 kg/cm^2, crashed, and sieved into 280–520 μm particles (Mesh = 30–50) [36–38]. The order of impregnation (first Pt and then Ba) was chosen to ensure good dispersion and stability of the precious metal and the alkaline component in the alumina base, according to Toyota's

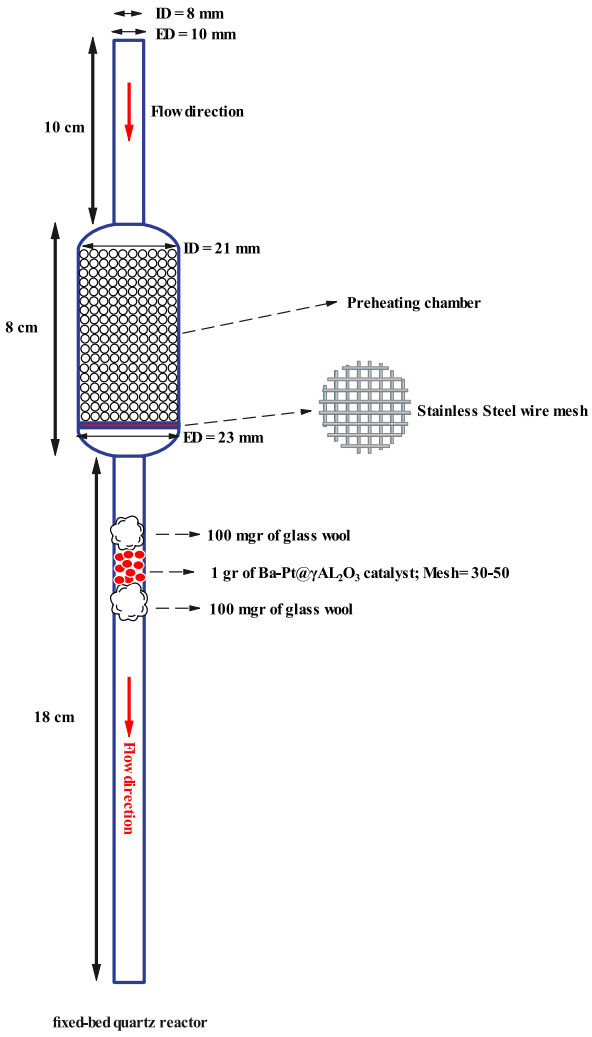

Fig. 1. The schematic of the quartz reactor with the preheating chamber.

patent guidelines [39].

2.3. Catalyst characterization

XRD patterns were obtained using an X'Pert MPD powder X-ray diffractometer to identify the phases and crystallographic structures. The instrument operated at 40 kV and 40 mA, with Cu Ka radiation ($\lambda = 0.154056$ nm), in the range of $5^\circ < \theta < 100^\circ$ and a step size of 0.02°. The average sizes of the crystallites were estimated using the Scherrer equation. Using a Micromeritics surface area and pore size analyzer, the N_2 adsorption-desorption isotherms were measured at −196 °C. All samples were degassed at 180 °C for 2 h before measurement. By employing the Brunauer-Emmett-Teller (BET) method, the specific surface area of the sample was determined. By utilizing a P/P_0 range of 0.01–0.99, the multipoint BET specific surface area was determined. The MIRA3 TESCAN FESEM with an EDX system (Oxford Inca) was used to conduct morphological analysis, elemental mapping, and semi-quantitative investigation of barium and platinum particles in the catalysts. Fourier Transform Infrared Spectrometer (FTIR) Model PERKIN ELMER Spectrom 2 was used to analyze the functional groups formed on the catalyst structure after the first and second impregnation on the support. Elemental analysis was carried out using inductively coupled plasma sector field mass spectrometry (ICP-OES 730-ES, Varian). Thermogravimetric analysis (TGA) was carried out using a TGA-DTG (SDT Q600 V20.9 Built 20) instrument. A catalyst sample of 5 mg and 60 ml/min flow of pure Ar was used with a heating rate of 10 °C/min.

2.4. Experimental design and optimization

Empirical approaches or statistical methods can be applied to process optimization. A drawback of the empirical approach is that it takes a long time to process, and the optimized parameters might need to be more precise [40]. The purpose of the experiment design in this research is to investigate the effect of the most critical operational and design variables. Also, with the experimental design method, it is possible to simultaneously examine the effect of the influential variables and the mutual influence that they may have on each other, as well as to optimize their values by conducting minimal experiments. In addition, in terms of time and cost of experiments, it is economical compared to the method of examining the effect of each variable separately, and a better understanding of the process is obtained [41].

The study meticulously focused on four critical variables for the quartz reactor with a preheating chamber, each significantly influencing the system's performance. These parameters were selected based on their known or expected influence on the reactor's performance, supported by literature [42–51] and preliminary experiments. The levels for each variable were carefully chosen to cover a wide range, including extreme and central values, to capture both linear and quadratic effects. The reactor outer wall temperature (Variable A) is crucial as it directly affects the thermal conditions within the reactor, influencing reaction kinetics and efficiency. A study shows that the performance of NSR catalysts peaks within the temperature range of 350–550 °C [43]. Another study reports that NSR catalysts can operate within the temperature range of 100–500 °C, but their performance varies depending on gas composition and specific conditions [42]. Additionally, results indicate that the optimal performance of these catalysts may be reduced at temperatures below 400 °C due to limitations in the storage process and NOx reduction [45]. Therefore, for a more comprehensive investigation of NSR catalysts in future research, the reactor outer wall temperature was examined within 50–600 °C. Moreover, gas hourly space velocity (GHSV) ranges for GDI engine catalysts are typically around 10,000 to 70,000 h^{-1} (h^{-1}) [46–48]. Of course, higher values have also been reported in harsh operating conditions [49,50]. This value can vary depending on the engine's working conditions and the type of catalyst. GHSV is one of the critical factors in determining the efficiency of catalytic conversion in reducing emissions from the exhaust of GDI vehicles [46–48]. The volumetric flowrate with levels from 0.3 L/min to 3 L/min, corresponds to a gas hourly space velocity of approximately 9000–90000 h^{-1}, and it determines the residence time of carrier gas in the preheating chamber and reactor, impacting the gas and catalyst temperature and also pressure drop in the preheating chamber and should be assessed to determine the relationship between this parameter and responses. Moreover, optimizing the volumetric flow rate is crucial for maintaining thermal efficiency, minimizing pressure drops, and ensuring the effective operation of the reactor. Proper control of these parameters contributes to improved reactor performance and energy efficiency. In addition, the wall temperature time (Variable C) spans from 0.16 min to 10 min and is the duration over which the reactor wall maintains a specific temperature. This period occurs after the outer wall of the reactor at point A on the preheating chamber reaches the desired temperature. It is a crucial step before assessing catalyst performance in the experimental tests, as it allows the reactor to reach steady-state conditions (gas and catalyst temperature) before assessment of NSR catalyst performance. Finally, the surface area of granules (Variable D), which ranges from 0 to 280 cm^2, is vital as it influences the contact area available for the heat transfer, thereby affecting the overall gas and catalyst temperature and the pressure drop in the preheating chamber. Therefore, the importance of these variables should be considered, as they significantly impact the overall performance of the reactor. In the present study, the statistical analysis of operational-design variables affecting pressure drop and temperature was performed using the Stat-Ease software version 13.0.5.0. The RCCD (Rotatable Center Composite Design) was applied to analyze the interactions among the design and process variables and to identify the optimum condition. The Central Composite Design (CCD) was chosen for this study because it offers a robust framework for exploring the relationships between multiple factors and their interactions, particularly in cases where quadratic effects are expected and mitigate or eliminate systematic errors. CCD is incredibly efficient in requiring fewer experimental runs than full factorial designs while still providing sufficient data to model second-order interactions. This design also allows for the generation of reliable response surfaces that can be used for optimization. Given the complexity and non-linearity of the system under investigation, CCD was considered the most appropriate method to capture accurately the effects of the independent variables on the response(s) [52,53]. Response Surface Methodology (RSM) is a set of mathematical statistical methods to develop, improve, save time and cost and optimize processes by

finding the correct relationship between the response and the independent fundamental factors. The RSM consists of a series of consecutive tests and is a method to determine the relationship between experimental parameters and observations [54]. Statistical modeling and optimization of gas and catalyst temperature and pressure drop of the reactor with the preheating chamber with fundamental and independent factors of external wall temperature, time, flowrate and granules surface area were investigated by Central Composite Design (CCD). In this research, the mutual influence of the fundamental factors was analyzed and investigated and ANOVA statistical analysis was performed to check the significance of the model and parameters. Moreover, the model verification test was performed after predicting the optimal condition by the software.

Following the design processes and the gathering of experimental data, an empirical model was created using the RSM approach. The polynomial function was initially fitted with the data before the factor values were identified to optimize the objective function. The coefficient of determination R^2 and R^2adj in Equations (1) and (2) were used to assess the precision of the fitted polynomial model:

$$R^2 = 1 - \frac{SSQ_{residual}}{SSQ_{mod} + SSQ_{residual}} \tag{1}$$

$$R^2_{adj} = 1 - \frac{SSQ_{residual}/DgF_{residual}}{(SSQ_{mod} + SSQ_{residual})/(DgF_{mod} + DgF_{residual})} \tag{2}$$

The multiple responses of the gas and catalyst temperature and the pressure drop due to the preheating chamber were examined to determine the system's performance, and the mathematical Equation (3) for the composite design is as follows:

$$Y = \beta_0 + \sum_{i=1}^{k} \beta_i \chi_i + \sum_{i=1}^{k} \beta_{ii} \chi_i^2 + \sum_{i=1}^{k-1} \sum_{j=i+1}^{k} \beta_{ij} \chi_i \chi_j + \varepsilon \tag{3}$$

Where Y represents the response vector, accounting for the primary, pure-quadratic, and two-factor interaction effects, and represents the error vector. In this study, the experimental design data were subjected to regression and graphical analysis, and the statistical significance of the different equations produced was assessed. Regression analysis and three-dimensional response surface plots were used to predict the optimum conditions for each dependent variable. Additionally, the p-value is regarded as a feature to assess the significance level of all independent variables while also indicating the strength of interactions between all independent variables; the smaller the p-value, the greater the significance of the related variable. The impact of the second-order regression models was evaluated using ANOVA and F-value analysis. Equation (4) can be used to represent the computed F-value.

$$F = \frac{MnS_{RG}}{MnS_{RD}} \tag{4}$$

The nomenclature section may be used to reference the definitions of these terms. The F-value is calculated in the particular point of importance using the DgF-based F distribution for residual and regression. Regression coefficients are derived from these analyses based on their significance in relation to the p-value. The coefficient of variation (CV), which is calculated as the percentage of standard deviation over mean value (Equation (5)), reflects the extent of error of any model.

$$CV = \frac{SD}{mean} \times 100 \tag{5}$$

A model can be replicable if its CV is less than 10 %. Using preliminary tests and based on the study of past research and knowledge of the process, four factors including: reactor outer wall temperature, volumetric flowrate, time and granules surface area were considered as the most critical design-operational variables affecting the responses. First, by using preliminary tests, past experiences and screening, the range of each variable is specified. Then five levels of change for each variable are calculated by the software. Each level of variables has a real value and a dimensionless coded value. Five coded levels of each variable include -α, +1, 0, −1 and +α. Here, the value of α is equal to 2 obtained from Equation (6). Where k is the number of variables equal to 4 [41].

$$\alpha = 2^{k/4} \tag{6}$$

Equation (7) obtains the number of designed experiments, where k is the number of variables and Cp is the number of repetitions at the central point.

$$N = K^2 + (2 \times K) + Cp \tag{7}$$

The range and coded level of (minimum and maximum values of the fundamental factors) the reactor variables studied are listed in Table 2. The change levels of each variable include upper and lower axial points (+α and -α), central point (0) and upper and lower factorial points (+1 and −1). The coefficients of the model for the response have been determined using the multiple regression analysis approach in the RSM. The fitting characteristic was examined from the model's regression coefficients and determination. ANOVA was used to investigate the effects of the independent and interactive factors in the model's equation. In addition, it was used to figure out the response surface plots to determine the optimum condition of a parameter and to forecast the experimental results for the other parameters in combinations.

Table 2
Level of variables considered for the quartz reactor with preheating chamber.

S.NO	Variable	Name	Variable level				
			-α	−1	0	1	+α
1	A	Reactor outer wall temperature (°C)	50	187.5	325	462.5	600
2	B	Volumetric flowrate (L/min)	0.3	0.98	1.65	2.33	3
3	C	Wall temperature time (min)	0.16	2.62	5.08	7.54	10
4	D	Surface area of granules (cm^2)	0	70	140	210	280

2.5. Temperature and pressure drop measurement

The present study selected the most important parameters with a detailed understanding of the process. Therefore, the variables of the reactor outer wall temperature, Surface area of granules used in the preheating chamber, volumetric flowrate and the wall temperature time (after the temperature of the outer wall of the reactor at the point of A on the pre-heating chamber reaches the desired temperature in the tests) were investigated. Moreover, their effect on the response variables (temperature before the catalyst, center of catalyst temperature and pressure drop due to the preheating chamber) was evaluated. Therefore, the design of the experiment was carried out as follows. The temperature was measured and monitored at 3 points: A (temperature of the reactor wall at a distance of 12 cm from the reactor inlet), B (gas temperature 1 cm before entering the catalyst), and C (center of catalyst temperature; 2 cm after the beginning of the reactor outlet pipe).

All temperatures were measured by K-type thermocouple (L = 20 cm and D = 1 mm). In addition to the placement of glass wool insulation at the B point in a cylindrical shape as shown in Fig. 2. [34], an aluminum cover was also configured at the outer reactor wall to exclude radiation from the electrical furnace and packed bed to the thermometer measuring the gas temperature. Also, the pressure difference before and after the reactor was measured by a micro manometer Model AIRFLOW EDM2500. The gas flow rate entering the reactor was adjusted using rotameter model LZB-4WB calibrated by a soap bubble flowmeter and digital calibrator. The fluid (Argon) entered the reactor at a lower temperature than that in the furnace, and then it was heated and flowed through the preheating chamber. Before entering the packed bed, the argon gas passed successively through several screen sheets, obtaining uniform flow and temperature distributions. The temperature of the inlet gas was measured by the thermocouples located about 25 mm above the entrance of the bed. The range of the inlet gas temperature was from 15 to 20 °C. It should be noted that temperature and pressure corrections were also applied. The setup of experiments is shown in Fig. 2.

3. Results and discussion

3.1. Catalysts characterization

Fig. 3 shows the XRD patterns of the γ-Al_2O_3, Pt@γ-Al_2O_3, and Ba-Pt@γ-Al_2O_3 catalysts. XRD measurements performed over the

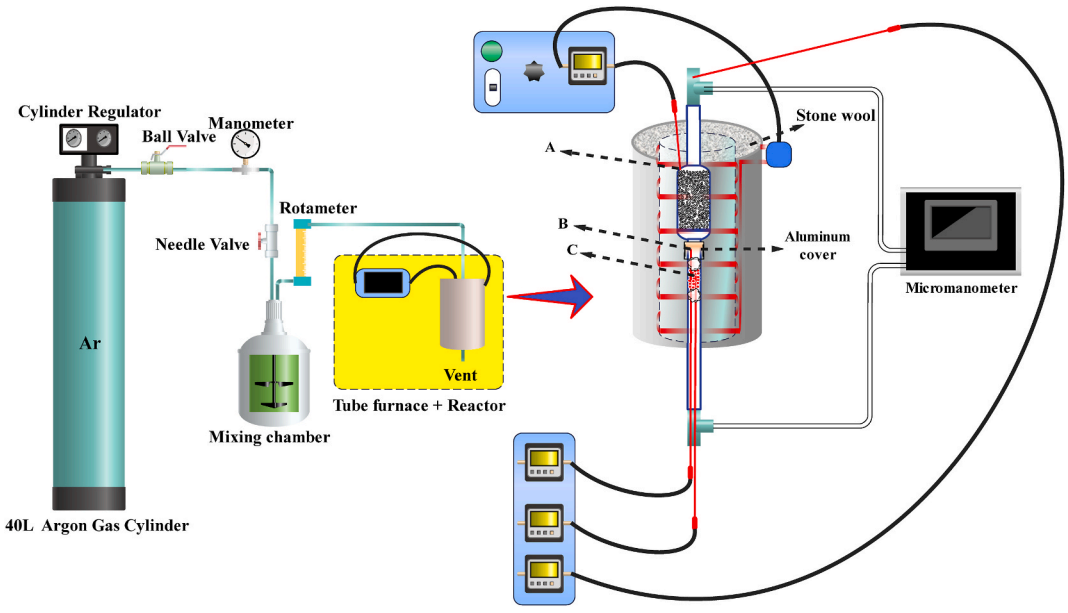

Fig. 2. Experimental setup of the study.

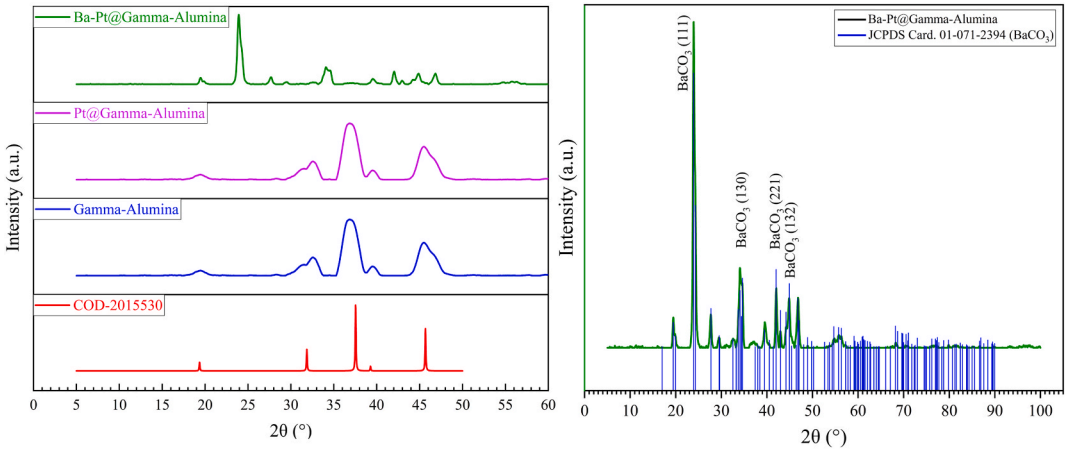

Fig. 3. XRD of calcined γ-Al_2O_3, Pt@γ-Al_2O_3 and Ba-Pt@γ-Al_2O_3

calcined samples revealed the presence of crystalline γ-Al_2O_3 (COD[1] cif n. 2015530), with a mean crystallite dimension (estimated by the Scherrer equation) of 4.88 nm. No Pt crystalline phases were detected in the Pt@γ-Al_2O_3 (1/100 w/w) and Ba-Pt@γ-Al_2O_3 (1/20/100 w/w) samples, thus suggesting that the Pt phase is well-dispersed over the support. In the fresh Ba-Pt@γ-Al_2O_3 catalyst, in addition to γ-Al_2O_3, both the monoclinic (JCPDS 78–2057) and orthorhombic (whiterite, JCPDS 5–378) polymorphic forms of $BaCO_3$ were detected. The formation of the metastable monoclinic phase was likely induced by the fast and highly exothermic decomposition of Ba acetate catalyzed by Pt, as evidenced by TGA-DTA experiments reported elsewhere [36]. Quantitative analysis of the XRD spectra indicated that Ba is well dispersed on the surface of the ternary Ba-Pt@γ-Al_2O_3 catalyst.

Table 3 provides a comprehensive overview of the catalyst properties, including the detected phases, their mean crystal size, surface area, pore volume, and pore size. One of the most significant findings is the impact of the addition of Barium on the catalyst properties. After heating at various temperatures, the Langmuir Surface area of the commercial alumina sample was 326–372 m^2/g. In comparison, a lower value has been measured for the Pt@γ-Al_2O_3 (322 m^2/g) and a progressive decrease for the Ba-Pt@γ-Al_2O_3 sample (216 m^2/g) due to forming a large matrix. This surface area contraction was accompanied by changes in the pore volume, especially after incipient wetness impregnation of Pt@γ-Al_2O_3 with an aqueous solution of Barium acetate followed by drying and calcination at 500 °C (γ-Al_2O_3(0.33–0.35 cm^3/g), Pt@γ-Al_2O_3 (0.37 cm^3/g) and Ba-Pt@γ-Al_2O_3 (0.19 cm_3/g)). The pore size is 8–10 nm (see Table 3). It is evident that the addition of Barium significantly affects the catalyst's surface area and pore volume. It can be seen that the pore volume and pore size of Pt@γ-Al_2O_3 are slightly higher than γ-Al_2O_3, because of the high dispersity of the platinum on the support.

Fig. 4 (a–c) shows the FESEM images and size distribution (calculated by ImageJ 1.52v and OriginPRO SR19.9.0.225 software) of γ-Al_2O_3, Pt@γ-Al_2O_3, and Ba-Pt@γ-Al_2O_3 samples. The images have a 5 μm scale. These results were obtained by averaging the measurement of 100 individual microparticles on the images.

Clustering of microstructures of varying sizes and shapes has been detected. The intervention of Pt and Ba with γ-Al_2O_3 is depicted in Fig. 4 (b and c), showing uniformly arranged particles with an irregularly shaped aggregate on the surface. The Ba-Pt@γ-Al_2O_3 has many rugged parts on the surface due to the surface loading of Pt and Ba nanoparticles.

Adding the Pt and Ba to γ-Al_2O_3 has altered the size of the products. The γ-Al_2O_3 before impregnation shows that the microparticles appear as irregular and mixed sphere-like shapes along with an average Particle Size (PZ) of 2.49 ± 1.02 μm and Polydispersity Index (PDI) of 0.4. Importantly, PZ and PDI follow a distinct pattern of change: they decrease after the first impregnation (Pt@γ-Al_2O_3; PZ = 1.5 ± 0.25 μm and PDI = 0.16) and then increase after the second impregnation (Ba-Pt@γ-Al_2O_3; PZ = 3 ± 0.06 μm and PDI = 0.2).

The analysis of energy-dispersive X-ray spectroscopy (EDX) is a crucial technique that enables the determination of the elemental composition of a given sample. Furthermore, it is utilized to cartographically represent the horizontal dispersion of chemical constituents within the imaged region. As illustrated in Fig. 5, Ba-Pt@γ-Al_2O_3 microparticles were subjected to EDAX analysis and are composed of 46.45 % Oxygen (O), 40.26 % Aluminum (Al), 12.52 % Barium (Ba), and 0.76 % Platinum (Pt) by weight. Importantly, no other elemental impurities were detected, ensuring the purity of the sample.

Identifying Pt and Ba in the EDX spectrum suggests the successful synthesis of the Ba-Pt@γ-Al_2O_3, with these elements potentially serving as active sites on the surface of the resulting catalyst. The presence of Pt, Ba, Al, and O corroborated the XRD results and indicated the formation of Ba-Pt@γ-Al_2O_3. The homogeneity of the loading is demonstrated in Fig. 5, which shows the Al, O, Ba, and Pt contents of the Ba-Pt@γ-Al_2O_3. Moreover, ICP-OES analysis was used for elemental analysis of Ba-Pt@γ-Al_2O_3, and Al, Ba, and Pt weight loadings of the catalyst were 11.2 %, 15.8 %, and 0.8 %, which is in line with elemental analysis by EDX.

Fig. 6 presents the findings from our FT-IR measurements, which have significant implications for catalyst development. These

[1] Crystallography Open Database.

Table 3
Structural and morphological properties of the catalysts.

Catalyst	Phases	Mean crystatites size (nm)	BET Surface area (m^2/g)	Langmuir Surface area (m^2/g)	Pore volume (cm^3/g)	Mean Pore size (nm)
γ-Al_2O_3 (120 °C overnight)	γ-Al_2O_3	4.88	132	372	0.35	9.5
γ-Al_2O_3 (700 °C for 5 h)	γ-Al_2O_3	4.88	125	361	0.33	9.3
γ-Al_2O_3 (700 °C for 5 h + 250 °C for 5 h)	γ-Al_2O_3	4.88	127	326	0.35	9.1
Pt@γ-Al_2O_3 (1/100 w/w)	γ-Al_2O_3	4.88	121	322	0.37	10
Ba-Pt@γ-Al_2O_3 (1/20/100 w/w)	γ-Al_2O_3 $BaCO_3$ (monoclinic) $BaCO_3$ (orthorhombic)	15.12	82	216	0.19	8

measurements revealed that the activation at 500 °C of the samples previously calcined in the air caused extensive dehydration, dehydroxylation, and surface decarbonization of the catalysts. The only surface species that remained on all samples were small amounts of free hydroxyl species of various types at the broadband at 3500 cm^{-1} (OH stretching region) and carbonates bands present on the Pt@γ-Al_2O_3 and pure γ-Al_2O_3 samples at 1600-1300 cm^{-1}. Notably, the activation treatment under vacuum induced a marked decrease in intensity of the bands assigned to Ba carbonate (1435 cm^{-1} with shoulders at 1323 and 1607 cm^{-1}) in the case of the Ba-Pt@γ-Al_2O_3. These findings strongly suggest the presence of Ba-Pt@γ-Al_2O_3 in the activated samples, which could have significant implications for catalyst performance.

The TG and DTG profile of the Ba-Pt@γ-Al_2O_3 is depicted in Fig. 7. The DTG profile displays three distinct thermal decomposition events, each characterized by peaks at 766 °C, 836 °C, and 1000 °C, respectively. This shows three thermally different species. The research conducted by Piacentini et al. [55] revealed the observation of two thermal decomposition events. The decomposition of LT-$BaCO_3$ into BaO is responsible for the low-temperature decomposition event. The high-temperature event is associated with the decomposition of the HT-$BaCO_3$ sites. However, Scholz et al. [56] proposed the distinction of three distinct barium species: amorphous BaO, amorphous LT-$BaCO_3$, and crystalline HT-$BaCO_3$. The thermal stability of these species relies on their interaction with the alumina support and Pt sites. Upon exposure to the atmosphere, the catalyst will initiate a reaction wherein BaO reacts with atmospheric CO_2, ultimately forming $BaCO_3$, which possesses low thermal stability [55]. This observation may explain three weight loss events in the DTG curve. The first two events are ascribed to the decomposition of a dispersed LT phase. The high-temperature event is ascribed to crystalline, bulk HT barium site decomposition.

3.2. Verification on statistical models

According to the CCD and based on Equation (7), the total number of experiments required is 30 runs (3 repetitions were conducted in each run) as shown in Table 4. The independent variables considered important in this process were: reactor outer wall temperature (A), volumetric flowrate (B), time (C), and granule surface area (D), for which the experiments were conducted to obtain the multiple responses, i.e., gas temperature (R_1), catalyst temperature (R_2) and pressure drop (R_3). 30 runs with various combinations of the reactor variables were performed in the experiments. Table 4 lists of the combination factors (resulted from CCD) suggested for the experimental design and the responses. These responses were used to validate and verify the mathematical model of the process to utilize newly designed quartz reactor. Experimental results showed that the gas temperature, catalyst temperature and pressure drop ranged from 31 to 177 °C, 51–585 °C and 7–153 Pa, respectively (Table 4).

3.3. Mathematical modeling and regression analysis

The responses, *gas* temperature before the catalyst, catalyst temperature, and pressure drop were assessed for the different mathematical models. The quadratic and 2FI (2 Factor Interaction) models matched the experimental data well, as evidenced by the regression value in the model summary statistics provided in Tables 5–7. Consequently, quadratic and 2FI models were adopted to determine how responses changed as the independent variables and their interactions changed. Equation (8) gives a generic representation of the quadratic model as follows:

$$Y = \beta_0 + \sum_{i=1}^{k} \beta_i \chi_i + \sum_{i=1}^{k} \beta_{ii} \chi_i^2 + \sum_{i=1}^{k-1} \sum_{j=i+1}^{k} \beta_{ij} \chi_i \chi_j + \varepsilon \quad (8)$$

Where Y is the predicted response, β_0 is the coefficient of the intercept, β_i is the coefficient of the linear terms, β_{ii} is the coefficient of the squared terms, β_{ij} is the coefficient of the interaction terms, and X_i, X_j are the coded independent variables.

The regression equation for the quadratic and 2FI models are respectively provided as follows (Equation (9) and (10)), taking into account the four independent variables in the current study:

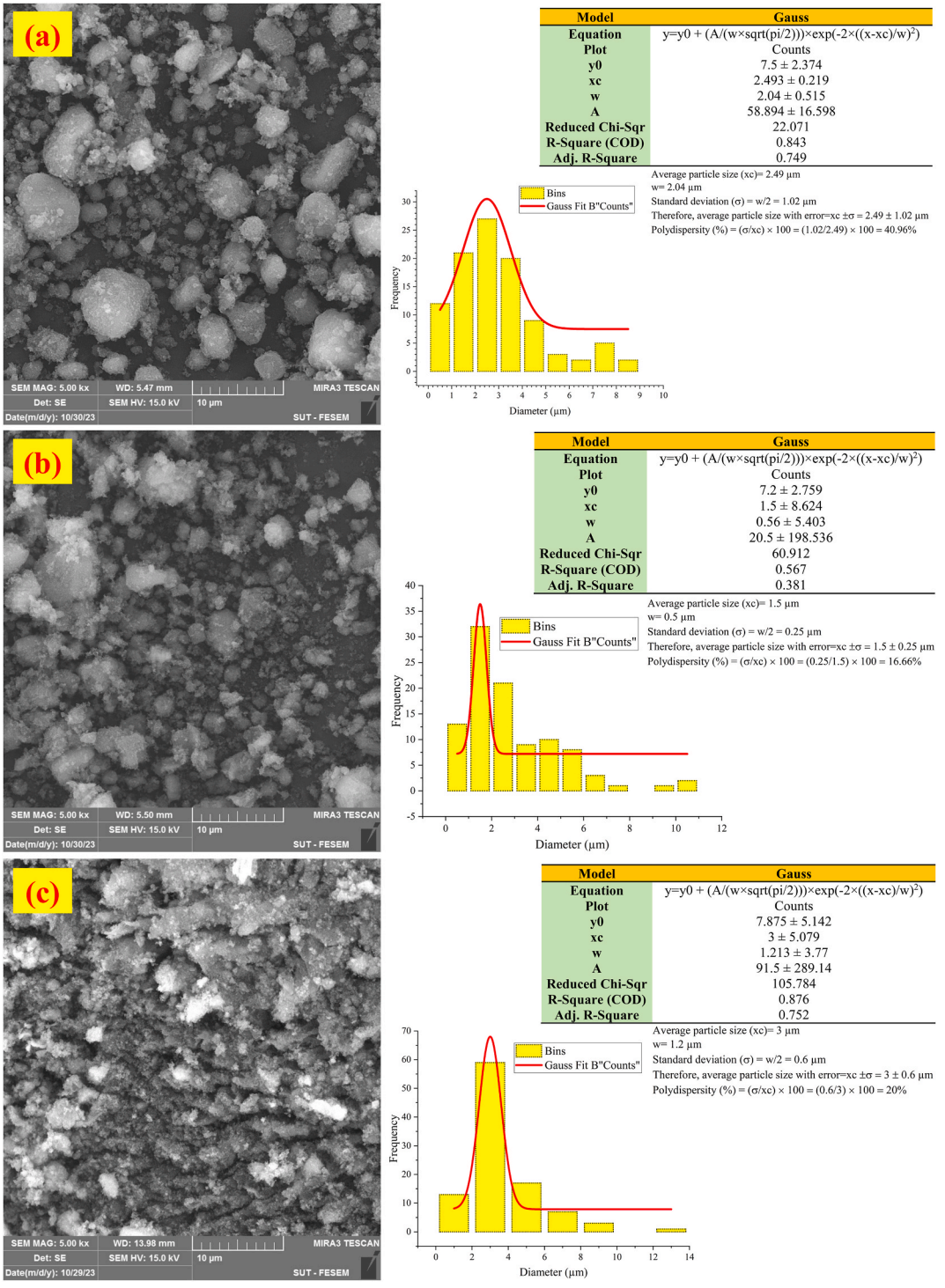

Fig. 4. (a)–(c) FESEM images and gaussian distribution of γ-Al_2O_3, Pt@γ-Al_2O_3 and Ba-Pt@γ-Al_2O_3, respectively.

$$Y = \beta_0 + \beta_1 X_1 + \beta_2 X_2 + \beta_3 X_3 + \beta_4 X_4 + \beta_{11} X_1^2 + \beta_{22} X_2^2 + \beta_{33} X_3^2 + \beta_{44} X_4^2 + \beta_{12} X_1 X_2 + \beta_{13} X_1 X_3 + \beta_{14} X_1 X_4 + \beta_{23} X_2 X_3 + \beta_{24} X_2 X_4 + \beta_{34} X_3 X_4 + \varepsilon \quad (9)$$

$$Y = \beta_0 + \beta_1 X_1 + \beta_2 X_2 + \beta_3 X_3 + \beta_4 X_4 + \beta_{12} X_1 X_2 + \beta_{13} X_1 X_3 + \beta_{14} X_1 X_4 + \beta_{23} X_2 X_3 + \beta_{24} X_2 X_4 + \beta_{34} X_3 X_4 + \varepsilon \quad (10)$$

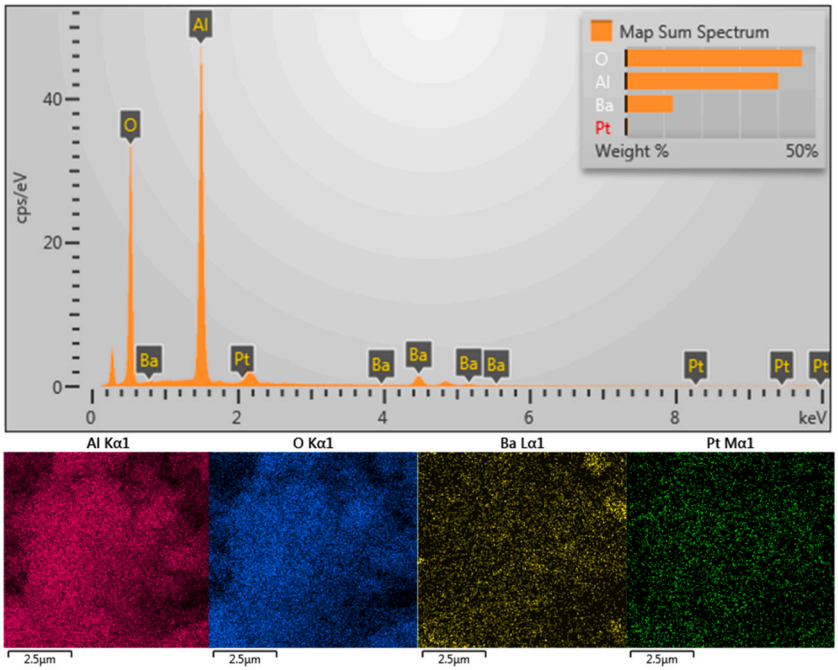

Element	Line Type	k Ratio	Wt. %	Wt. % Sigma	Atomic %	Standard Label
O	K series	0.02852	46.45	0.21	64.65	SiO^2
Al	K series	0.03882	40.26	0.19	33.23	Al_2O_3
Ba	L series	0.01177	12.52	0.21	2.03	BaF_2
Pt	M series	0.00063	0.76	0.21	0.09	Pt
Total:			100		100	

Fig. 5. EDX analysis, mapping and elemental composition (wt. %) of Ba-Pt@γ-Al_2O_3

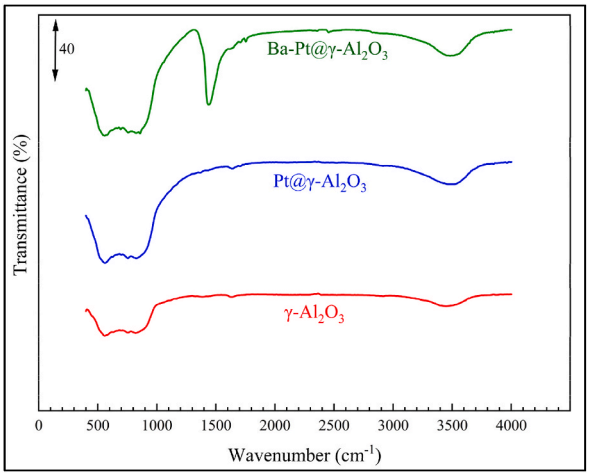

Fig. 6. FTIR transmittance spectra of γ-Al_2O_3, Pt@γ-Al_2O_3, and Ba-Pt@γ-Al_2O_3 calcined at 500 °C.

Tables 5–7 show that the quadratic and 2FI models are the best-fit models in terms of significance. The 2nd order (response 1 and 2) and Interaction (response 3) models are recommended for this experimental design since their p-values are also smaller than those of other models. As can be seen in Table 5, the linear model explains 86.78 % of the variance in gas temperature, indicating a good fit to the data. However, the lower predicted R^2 compared to R^2 and adjusted R^2 suggests a slight reduction in the model's predictive power, which may imply some limitations in forecasting new data. The 2FI model provides a very good explanation of the variance in gas

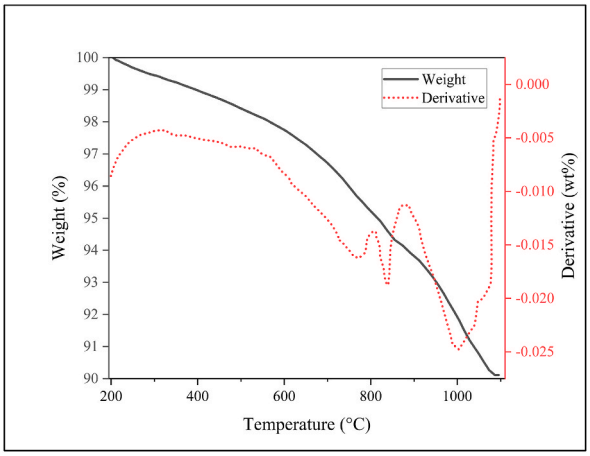

Fig. 7. TGA-DTG profile of Ba-Pt@γ-Al_2O_3

temperature, with a high predicted R^2, indicating strong predictive capability. The lower PRESS value compared to the linear model suggests improved accuracy in prediction. The quadratic model demonstrates an excellent fit to the data, with high R^2 and adjusted R^2 values and a predicted R^2 close to R^2. The low PRESS value indicates strong predictive performance and suggests this model is highly reliable. However, the cubic model, despite exhibiting very high R^2 and adjusted R^2 values, has extremely low predicted R^2 and very high PRESS, which clearly suggests issues with model predictability. This model may not be suitable for accurate prediction of new data. Therefore, the quadratic model is recommended for gas temperature due to its superior performance in explaining the variance and strong predictive accuracy. Similarly, detailed interpretations of model performance and predictive accuracy, as discussed in Table 5, are applicable to the results presented in Tables 6 and 7, providing a consistent framework for evaluating the various models for catalyst temperature and pressure drop.

3.4. Analysis of variance and development of regression model equation

In the current work, a CCD for four variables (e.g., reactor outer wall temperature, flow rate, time, and granule surface area, each with five levels (Table 2) was used to design the model. To evaluate the 15 coefficients of the quadratic equation and 11 coefficients of the 2FI equation, 30 experimental runs were conducted on the system for each of the responses, namely gas temperature, catalyst temperature and pressure drop.

The model summary statistics (Tables 5–7) suggested fitting of a quadratic and 2FI models based on the significance of the adjusted R^2 value, with additional terms in the model and higher model aliased. Furthermore, it is observed from Tables 5–6 that the quadratic and 2FI models are the best-fit models in terms of their significance and for this experimental design, as the p-value of this model is also smaller than that of other models.

The multiple regression analysis technique in the RSM was used to determine the coefficients of the quadratic and 2FI model.

F-value and p-value analyses were used as a result of the analysis of variance (ANOVA) approach. Tables 8–10 show the results of the ANOVA performed for the quadratic, quadratic and 2FI models for the gas temperature, catalyst temperature and pressure drop, respectively.

If the p probability value in Fischer's F-statistics be low, the regression model is discovered to be very significant. While the interaction of the various variables can be determined from the p values, the significance of the regression coefficients of the parameters was confirmed using the Student's t-test. When the corresponding value of t is high and the corresponding value of p is low, a coefficient is said to be significant [40,57].

Small p-values (Prob > F) show that certain model terms can improve the model's significance. The models also relate to the F-value. A smaller value implies that the variance may be more attributable to noise, whereas a bigger F-value shows that the model can explain more of the variance.

The models were determined to be significant from the ANOVA for responses since the probability p-value was less than 0.05. According to p-values, the model terms were significant if probability > F and less than 0.05.

As a result, in Table 8, the terms A, B, and AB were highly significant and the terms C, D, A^2, B^2 and D^2 were moderately significant in the model Equation (11) to signify the individual and interactive effects of the variables on gas temperature due to preheating chamber. All other terms, e.g., AC, AD, BC, BD, CD and C^2 were insignificant and emitted from the final Equation of (11) and (14). Similarly, according to Tables 9 and 10, the insignificant terms were removed, so as highly and moderately significant terms create final regression Equation of (12), (13), (15), and (16) to predict the catalyst temperature and pressure drop explaining the individual and interactive effects of the variables on the response.

For the proposed quadratic and 2FI equations, the matched independent factors were also tested for the integrity of fit. Numerous indicators were used to evaluate the suitability of the fitted model, and the results are shown in Tables 8–11. Indicators such as R^2, R^2_{adj},

Table 4
Independent variables and results for the quartz reactor with preheating chamber by the CCD.

Run order	Std order	Coded variable				Actual variable				Responses					
		A	B	C	D	A	B	C	D	R_1		R_2		R_3	
										Actual	Predicted	Actual	Predicted	Actual	Predicted
1	15	−1	1	1	1	187.5	2.325	7.54	210	76	75.13	216	224.29	58	59.87
2	2	1	−1	−1	−1	462.5	0.975	2.62	70	61	55.29	492	491.46	24	20.03
3	9	−1	−1	−1	1	187.5	0.975	2.62	210	50	46.79	210	211.63	18	12.2
4	6	1	−1	1	−1	462.5	0.975	7.54	70	65	65.96	487	484.08	24	20.03
5	1	−1	−1	−1	−1	187.5	0.975	2.62	70	36	39.13	213	214.42	8	14.2
6	27	0	0	0	0	325	1.65	5.08	140	73	77	381	387	47	48.2
7	13	−1	−1	1	1	187.5	0.975	7.54	210	40	43.96	220	217.75	18	12.2
8	30	0	0	0	0	325	1.65	5.08	140	78	77	386	387	49	48.2
9	21	0	0	−2	0	325	1.65	0.16	140	54	63.42	382	378.63	44	48.2
10	20	0	2	0	0	325	3	5.08	140	141	151.75	402	392.79	84	91.37
11	4	1	1	−1	−1	462.5	2.325	2.62	70	153	146.46	504	508.75	55	58.7
12	28	0	0	0	0	325	1.65	5.08	140	83	77	383	387	48	48.2
13	12	1	1	−1	1	462.5	2.325	2.62	210	167	160.63	479	482.96	153	144.7
14	8	1	1	1	−1	462.5	2.325	7.54	70	167	163.63	486	492.13	55	58.7
15	10	1	−1	−1	1	462.5	0.975	2.62	210	70	67.96	450	451.92	56	60.03
16	17	−2	0	0	0	50	1.65	5.08	140	31	28.92	51	47.46	14	2.87
17	7	−1	1	1	−1	187.5	2.325	7.54	70	73	72.46	201	201.58	22	15.87
18	16	1	1	1	1	462.5	2.325	7.54	210	177	171.29	477	478.08	153	144.7
19	19	0	−2	0	0	325	0.3	5.08	140	31	29.42	370	368.96	7	5.03
20	25	0	0	0	0	325	1.65	5.08	140	75	77	395	387	44	48.2
21	24	0	0	0	2	325	1.65	5.08	280	95	100.75	326	316.46	84	90.2
22	18	2	0	0	0	600	1.65	5.08	140	130	141.25	585	578.29	104	93.53
23	5	−1	−1	1	−1	187.5	0.975	7.54	70	43	42.79	205	208.79	8	14.2
24	26	0	0	0	0	325	1.65	5.08	140	81	77	387	387	41	48.2
25	22	0	0	2	0	325	1.65	10	140	78	77.75	375	368.13	44	48.2
26	14	1	−1	1	1	462.5	0.975	7.54	210	75	72.13	447	456.29	56	60.03
27	29	0	0	0	0	325	1.65	5.08	140	72	77	390	387	40	48.2
28	23	0	0	0	−2	325	1.65	5.08	0	82	85.42	334	333.29	8	6.2
29	11	−1	1	−1	1	187.5	2.325	2.62	210	75	71.46	222	227.42	58	59.87
30	3	−1	1	−1	−1	187.5	2.325	2.62	70	66	62.29	218	216.46	22	15.87

Table 5
Model summary statistics–response 1–gas temperature.

Source	Std. Dev.	R^2	Adjusted R^2	Predicted R^2	PRESS	Comments
Linear	16.01	0.867	0.846	0.796	9843.08	
2FI	9.23	0.966	0.949	0.919	3919.22	
Quadratic	**6.91**	**0.985**	**0.971**	**0.923**	**3706.08**	**Suggested**
Cubic	7.23	0.992	0.968	0.2	38745.12	Aliased

Note: FI=Factorial Interaction; Std. Dev = Standard Deviation; PRESS=Predicted Sum of Square.

Table 6
Model summary statistics–response 2–catalyst temperature.

Source	Std. Dev.	R^2	Adjusted R^2	Predicted R^2	PRESS	Comments
Linear	26.08	0.961	0.955	0.946	23634.7	
2FI	28.10	0.966	0.948	0.936	28116.04	
Quadratic	**6.93**	**0.998**	**0.996**	**0.991**	**3604.32**	**Suggested**
Cubic	8.18	0.998	0.995	0.887	49537.44	Aliased

Note: FI=Factorial Interaction; Std. Dev = Standard Deviation; PRESS=Predicted Sum of Square.

Table 7
Model summary statistics–response 3–pressure drop.

Source	Std. Dev.	R^2	Adjusted R^2	Predicted R^2	PRESS	Comments
Linear	15.76	0.845	0.821	0.76	9637.84	
2FI	**7.12**	**0.976**	**0.963**	**0.919**	**3246.47**	**Suggested**
Quadratic	6.25	0.985	0.971	0.923	3072.72	
Cubic	3.23	0.998	0.992	0.99	402	Aliased

Note: FI=Factorial Interaction; Std. Dev = Standard Deviation; PRESS=Predicted Sum of Square.

Table 8
ANOVA for response surface quadratic model for gas temperature [Equation (11)].

Source	Sum of Squares	df	Mean Square	F-value	p-value	
Model	47493.62	8	5936.7	131.47	<0.0001	significant
A-Reactor outer wall temperature	18928.17	1	18928.17	419.18	<0.0001	
B-Volumetric flowrate	22448.17	1	22448.17	497.14	<0.0001	
C-Wall temperature time	308.17	1	308.17	6.82	0.016	
D-Surface area of granules	352.67	1	352.67	7.81	0.01	
AB	4624	1	4624	102.4	<0.0001	
A^2	141.75	1	141.75	3.14	0.09	
B^2	367.94	1	367.94	8.15	0.009	
D^2	505.75	1	505.75	11.2	0.003	
Residual	948.25	21	45.15			
Lack of Fit	850.25	16	53.14	2.71	0.137	not significant
Pure Error	98	5	19.6			
Cor Total	48441.87	29				

CV, and F values were employed to assess the model's suitability [58]. According to Tables 8–10, the F-value of the models at 131.47, 814.46, and 156.62 indicates the significance of these models, showing negligible tendency towards noise [59,60]. The p-value was very low (p-value<0.0001) since less than 0.05 for the p-value shows that the model terms chosen are greatly important. The suggested models' precision and accuracy may be evaluated using the coefficient of determination (R^2 value). The obtained results of 0.9804, 0.9973, and 0.9761 for R_1 (gas temperature), R_2 (catalyst temperature), and R_3 (pressure drop) indicate that just 1.96 %, 0.27 %, and 2.39 % of the total changes are unclarifiable, and 98.04 %, 99.73 %, and 97.61 % of the variability in the responses can be explained by the models [61,62]. Moreover, the obtained values of the adjusted determination coefficient (R^2_{adj}) are 0.9730, 0.9961, and 0.9699 indicating a good relationship among the independent factors. Here, low values of CV (8.07 %, 2.18 %, and 13.42 %) demonstrated a high degree of accuracy and an outstanding consistency of the models for the experimental results.

As can be seen in Table 8, all of the linear components (A, B, C, and D) were significant model terms because of their low p-values. Table 8 illustrates that the linear effects of the variables A ($p < 0.0001$), B ($p < 0.0001$), C ($p = 0.016$), and D ($p = 0.01$) on the gas temperature response were significant since the probability p-value is less than 0.05 and in which the variable A (F-value of 419.18) and B (F-value of 497.14) were found to be highly significant. The interaction effects of the AB ($F = 102.40$, $p < 0.0001$) term on the gas temperature response were also highly significant, indicating a combined effect of reactor outer wall temperature and volumetric flow rate on the gas temperature. The Lack of Fit is not significant ($p = 0.137$), suggesting that the model adequately fits the data

Table 9
ANOVA for response surface quadratic model for catalyst temperature [Equation (12)].

Source	Sum of Squares	df	Mean Square	F-value	p-value	
Model	4.399E+5	9	48880.5	814.46	<0.0001	significant
A-Reactor outer wall temperature	4.227E+5	1	4.227E+5	7042.77	<0.0001	
B-Volumetric flowrate	852.04	1	852.04	14.2	0.001	
C-Wall temperature time	165.38	1	165.38	2.76	0.112	
D-Surface area of granules	425.04	1	425.04	7.08	0.015	
AB	232.56	1	232.56	3.88	0.063	
AD	1350.56	1	1350.56	22.5	0.0001	
A^2	9389.73	1	9389.73	156.45	<0.0001	
C^2	284.48	1	284.48	4.74	0.041	
D^2	6565.23	1	6565.23	109.39	<0.0001	
Residual	1200.31	20	60.02			
Lack of Fit	1074.31	15	71.62	2.84	0.126	not significant
Pure Error	126	5	25.2			
Cor Total	4.411E+5	29				

Table 10
ANOVA for response surface quadratic model for pressure drop [Equation (13)].

Source	Sum of Squares	df	Mean Square	F-value	p-value	
Model	39343.83	6	6557.31	156.62	<0.0001	significant
A-Reactor outer wall temperature	12330.67	1	12330.67	294.51	<0.0001	
B-Volumetric flowrate	11180.17	1	11180.17	267.03	<0.0001	
D-Surface area of granules	10584	1	10584	252.79	<0.0001	
AB	1369	1	1369	32.7	<0.0001	
AD	1764	1	1764	42.13	<0.0001	
BD	2116	1	2116	50.54	<0.0001	
Residual	962.97	23	41.87			
Lack of Fit	892.13	18	49.56	3.5	0.085	not significant
Pure Error	70.83	5	14.17			
Cor Total	40306.8	29				

Table 11
Standard deviation and R^2 for R_1 (Gas temperature), R_2 (Catalyst temperature) and R_3 (Pressure drop).

Response	Gas temperature (K̇)	Catalyst temperature (K̇)	Pressure drop (Pa)
Std. Dev.	6.72	7.75	6.47
Mean	83.27	355.8	48.2
C.V. %	8.07	2.18	13.42
R^2	0.98	0.997	0.976
Adjusted R^2	0.973	0.996	0.969
Predicted R^2	0.946	0.992	0.956
Adeq Precision	38.139	118.682	45.378

without significant unexplained variance.

The findings in Table 9 showed that the model is highly significant, with an F-value of 814.46 and a p-value of <0.0001, indicating that it accurately predicts catalyst temperature. Moreover, it demonstrates that except for variable C, other linear components (A, B, and D) were significant model terms because of their low p-value. Similarly, from Tables 9 and it was observed that the linear effects of the variables A ($p < 0.0001$), B ($p = 0.001$), and D ($p = 0.015$) on the catalyst temperature response were significant and in which variable A was found to be highly significant (This factor is extremely significant, with an F-value of 7042.77 and a p-value of <0.0001, reflecting its dominant influence on catalyst temperature); besides the squared terms, A^2 ($p < 0.0001$) and D^2 ($p < 0.0001$) were also found to have highly significant effects on the catalyst temperature. In addition, C^2 ($p = 0.0416$) has a moderately significant effect on the catalyst temperature, indicating non-linear effects (A^2, C^2, and D^2) are important in modeling catalyst temperature. It is worse to note that the Lack of Fit is not significant ($p = 0.1269$), indicating that the model provides an appropriate fit to the data.

As shown in Table 10, the model is highly significant, with an F-value of 156.62 and a p-value of <0.0001, demonstrating its effectiveness in explaining the variation in pressure drop. It should be noted that except for variable C, all linear and interaction effects of variables ($p < 0.0001$) on the pressure drop response were highly statistically significant. Across all three models, reactor outer wall temperature and volumetric flow rate consistently emerge as the most influential factors, with highly significant effects on the respective responses. The surface area of granules also plays a critical role, especially in pressure drop. The models show a good fit to the experimental data, with non-significant Lack of Fit values, supporting their reliability in capturing the underlying processes.

Equations (11)–(13) represent the quadratic and two-factor interaction (2FI) models for gas temperature, catalyst temperature, and

pressure drop, expressed in terms of coded factors. Each equation highlights the relationship between the coded independent variables and the respective response.

$$\text{Gas temperature} = 28.08\ A + 30.58\ B + 3.58\ C + 3.83\ D + 17\ AB + 2.25\ A^2 + 3.63\ B^2 + 4.25\ D^2 + 75.17 \quad (11)$$

$$\text{Catalyst temperature} = 132.71\ A + 5.96\ B - 2.63\ C - 4.21\ D + 3.81\ AB - 9.19\ AD - 18.31\ A^2 - 3.19C^2 - 15.31\ D^2 + 385.25 \quad (12)$$

$$\text{Pressure drop} = 22.67\ A + 21.58\ B + 21\ D + 9.25\ AB + 10.5\ AD + 11.5\ BD + 48.2 \quad (13)$$

The negative and positive signs before the terms draw attention to an antagonistic and a synergistic effect [40]. In the context of Design-Expert software, the magnitude of the coefficients in coded equations indicates the relative impact of each factor on the response. Larger coefficients signify a more significant influence of the corresponding factor on the response. This relationship is beneficial for comparing the effects of different factors. However, in actual (uncoded) equations, due to differences in units and scales, direct comparison of coefficients may not accurately reflect the relative impact of factors. For instance, as seen in Equation (11), the positive coefficients of A and B suggest that increases in reactor outer wall temperature and volumetric flow rate significantly raise the gas temperature, with B having a slightly more robust influence. The interaction term AB indicates a substantial synergistic effect between A and B, further amplifying the gas temperature when both factors are increased simultaneously. The quadratic terms A^2, B^2, and D^2 indicate non-linear effects, particularly with B^2 and D^2, which contribute to an increase in gas temperature at higher levels of these factors. Moreover, in Equation (12), the catalyst temperature is primarily influenced by the reactor outer wall temperature (A), with the large coefficient of 132.71 indicating a dominant effect. The positive sign of B suggests a moderate increase in catalyst temperature with a higher volumetric flow rate. In Equation (13), the pressure drop within the system is influenced by the reactor outer wall temperature (A), volumetric flow rate (B), and surface area of granules (D), with all three factors contributing positively and almost equally to the pressure drop. The presence of interaction terms AB, AD, and BD indicates that the pressure drop is significantly affected by the combined effects of these factors. For instance, BD has the most significant interaction effect, suggesting that when both the volumetric flow rate and surface area of granules are high, the pressure drop increases considerably. The absence of quadratic terms in this model implies that the relationship between the pressure drop and these factors is primarily linear and interactive.

The quadratic and 2FI models in terms of actual factors are depicted in Equations (14)–(16).

$$\text{Gas temperature} = -0.175 \times \text{Reactor outer wall temperature} - 40.475 \times \text{Volumetric flowrate} + 1.456 \times \text{Wall temperature time} - 0.188 \times \text{Surface area of granules} + 0.183 \times \text{Reactor outer wall temperature} \times \text{Volumetric flowrate} + 0.0001 \times (\text{Reactor outer wall temperature})^2 + 7.956 \times (\text{Volumetric flowrate})^2 + 0.0008 \times (\text{Surface area of granules})^2 + 68.415 \quad (14)$$

$$\text{Catalyst temperature} = 1.66 \times \text{Reactor outer wall temperature} - 4.523 \times \text{Volumetric flowrate} + 4.284 \times \text{Wall temperature time} + 1.125 \times \text{Surface area of granules} + 0.041 \times \text{Reactor outer wall temperature} \times \text{Volumetric flowrate} - 0.0009 \times \text{Reactor outer wall temperature} \times \text{Surface area of granules} - 0.0009 \times (\text{Reactor outer wall temperature})^2 - 0.526 \times (\text{Wall temperature time})^2 - 0.003 \times (\text{Surface area of granules})^2 - 127.706 \quad (15)$$

$$\text{Pressure drop} = -0.152 \times \text{Reactor outer wall temperature} - 34.489 \times \text{Volumetric flowrate} - 0.456 \times \text{Surface area of granules} + 0.099 \times \text{Reactor outer wall temperature} \times \text{Volumetric flowrate} + 0.001 \times \text{Reactor outer wall temperature} \times \text{Surface area of granules} + 0.243 \times \text{Volumetric flowrate} \times \text{Surface area of granules} + 59.168 \quad (16)$$

The values of the predicted responses for the gas temperature, catalyst temperature, and pressure drop from Equations (14)–(16) are shown in Table 11. Table 11 presents a statistical summary of gas temperature, catalyst temperature, and pressure drop, including standard deviation, mean, C.V. (Coefficient of Variation), and R^2 values. The statistics provide information on the models' accuracy, reliability, and predictive ability for each response. The standard deviation reflects the dispersion of the gas temperature data around the mean. A relatively low standard deviation indicates that the predicted responses are closely clustered around the mean, suggesting good model precision. The standard deviation for catalyst temperature indicates a slightly higher dispersion than gas temperature and pressure drop, but it remains relatively low, suggesting good precision. The C.V. measures relative variability, indicating that the standard deviation is 8.07 % of the mean gas temperature. This low C.V. value suggests a stable and consistent model performance. The very low C.V. of R_2 indicates that the model's predictions for catalyst temperature are highly consistent, with only 2.18 % variability relative to the mean. The higher C.V. of R_3 compared to the other responses (R_1 and R_2) indicates greater relative variability in the pressure drop predictions, but it still reflects an acceptable level of model stability. The adequate precision values for R_1 (38.13), R_2 (118.68), and R_3 (45.37) indicate signal-to-noise ratios well above the desirable threshold of 4. These high values confirm the model's ability to navigate the design space effectively and ensure reliable exploration. Therefore, the statistical summary presented in Table 11 indicates that all three models exhibit high precision, reliability, and predictive power. The very high R^2, adjusted R^2, and predicted R^2 values, combined with low coefficients of variation and substantial adequate precision values, demonstrate that the models are well-suited for accurately predicting gas temperature, catalyst temperature, and pressure drop within the system.

Typically, it is crucial first to determine whether the fitted model accurately approximates the actual data. The integrated response surface must be further analyzed and optimized even while the model explains an acceptable fit to avoid producing inaccurate or misleading findings. Several diagnostic techniques were employed in the present study to evaluate the suitability and the process parameters. Influence plots and residuals (discrepancy between the expected and actual response values) also measured the models' suitability to determine the coefficient for the experimentally collected data. Residuals are typically thought of as parts of variations that have been imprecisely fitted to the model. As a result, it is expected that they would behave in a way consistent with a normal distribution characteristic. A graphical visualization of the normal probability plot has been considered as the proper method to

evaluate the normality of the residuals. When investigated residuals were plotted against projected values in this work, they lay logically near a straight line and showed no evidence of variance digression. This makes it possible to verify that the data are distributed normally.

Moreover, the regression models were used to calculate the predicted values of the responses compared with the experimental results shown in Fig. 8 (a, b and c). Fig. 8 illustrates the comparison between the gas temperature, catalyst temperature, and pressure drop obtained through the experiments and those predicted by Equations (14)–(16). Fig. 8 illustrates that experimental and predicted values dispersed close to the straight line have a suitable relationship. This demonstrates that the given regression equations were adequate for fitting the data, and that CCD models, in conjunction with the experimental design are effectively functional for optimizing the responses.

The values of the regression coefficient for Equations (14)–(16) are ($R^2 = 0.9804$), ($R^2 = 0.997$), and ($R^2 = 0.976$). They show that 1.96 %, 0.27 %, and 2.39 % of the response have not been satisfactorily predicted (Table 11) by the model Equations (14)–(16), respectively. For the responses provided in Tables 8–10, the ANOVA obtains the ratio of mean squares owing to regression and mean squares due to residual error, which aids in determining whether these terms have statistical significance. These tables clarify that all three of the response's F-statistics values had p-values less than 0.001, indicating that all responses can be effectively described by their respective model equations. In general, p-values lower than 0.001 generally show that the model is considered statistically significant at the 99 % confidence level [63].

It is desirable to utilize the RSM approach when the response is frequently affected by several factors concurrently. Effect plots may be used to display the impact of a variable on the response. The Pareto chart is one such plot that utilizes a bar graph to illustrate the

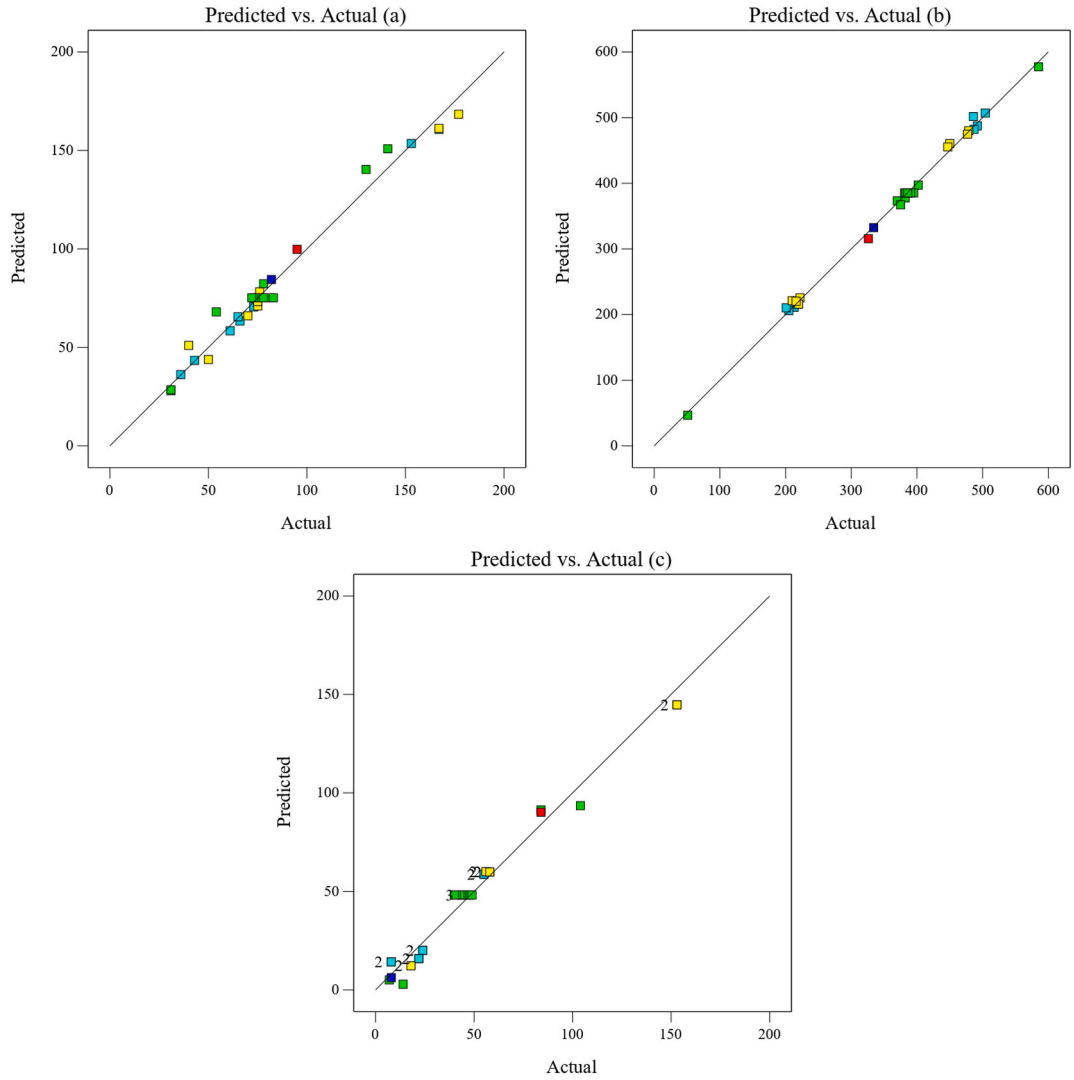

Fig. 8. Comparison plot between the actual and model predicted responses; (a) = Gas temperature, (b) = Catalyst temperature and (c) = Pressure drop.

effect, whether it be a factor or an interaction. The effect's magnitude is indicated by the size of the bar [40,64]. After eliminating the insignificant terms, Fig. 9 depicts the Pareto chart for the impact of the various factors and terms on the response, i.e., gas temperature, catalyst temperature, and pressure drop. Because of the considerable difference between F values obtained for different terms of the statistical models and the resulting difficulty in presenting a clear and differentiable graphical representation of data, all the X-axis values (F values) were plotted in the natural log (Ln) scale [65,66]. Larger values on top of the effects plot indicate that the related factors are more critical to the response. Additionally, the type of effect (positive or negative) on the desired response can be determined from the coefficient sign in Equations (11)–(13).

3.5. Interaction effects of variables using 3D response surface plots

The RSM method, with its unique ability to detect interactions between independent parameters and recognize the impacts of binary combinations, plays a significant role in our research. It effectively connects two independent factors and offers several advantages. Furthermore, the use of three-dimensional plots of the model enhances the graphical presentation of the interactions, making them easier to understand [67].

While the other independent parameters remained constant at their center point, the response surfaces can describe how the two other parameters interact. The color line levels in these figures depict the varied effects on the responses.

The 3D response surface plots effectively illuminate the various influences of the factors and their interactions on the responses. To further illustrate the individual and interactive effects of the variables on the responses within their prescribed ranges, the polynomial equations were utilized to create three-dimensional (3D) surfaces and two-dimensional (2D) contours. Fig. 10 (a and b), 11 (c and d) and 12 (e and f), 13 (g and h), 14 (i and j), and 15 (k and l) display the gas temperature, catalyst temperature, and pressure drop charts in 2D and 3D to illustrate the influence of important interactive factors. The graphs were shown as a function of two variables simultaneously, with the other variables remaining at their initial values.

As can be seen in Fig. 10, the contours and response surface plots showed that the gas temperature increased with the increase in reactor outer wall temperature and gas volumetric flow rate.

From Fig. 10 (a and b) and Tables 8 and it was seen that there existed a significant interaction between the reactor outer wall temperate and gas volumetric flowrate on the gas temperature; besides, the square terms of the variables (A^2, B^2, and D^2) were also significant (Table 8). The interaction term AB indicates a substantial synergistic effect between A and B, further amplifying the gas temperature when both factors are increased simultaneously. The same was also evident in Fig. 10 (a) from the curved contour lines, in which the gas temperature increased with an increase in the reactor outer wall temperate and gas volumetric flow rate to a certain extent.

Similarly, from Fig. 11 (c and d) and 12 (e and f), and Tables 9 and it was found that there existed significant interactions between the reactor outer wall temperature and volumetric flow rate (AB interaction; p-value = 0.063), as well as between the reactor outer wall temperature and surface area of granules (AD interaction; p-value = 0.0001) on the catalyst temperate. Besides, the squared terms of the reactor outer wall temperature (A^2; p-value<0.0001) and wall temperature time (C^2; p-value = 0.0416) and surface area of granules (D^2; p-value<0.0001) were also significant. It is interesting to note that in Fig. 11. (c), as shown by the slope of the contour lines, the effectiveness of the volumetric flow rate increases at higher outer wall temperatures.

The same could be confirmed from the curved contour lines of the plots, as the catalyst temperature increased with an increase in the reactor outer wall temperature to a certain extent and also increased proportionately with the increase in the volumetric flow rate (Fig. 11 (c)). Interestingly, the catalyst temperature increased with an increase in the surface area of granules and then decreased (Fig. 12 (e)). The maximum catalyst temperature at the higher reactor wall temperature tends to shift toward the lower quartz granules inside the preheating chamber. However, more quartz granules are needed at lower reactor wall temperatures for the same effect. Simply put, the effect of increasing the quantity of quartz granules in the preheating chamber on the catalyst temperature is dual and depends on the operating conditions. If the increased surface area of quartz granules for heat exchange is the dominant factor, catalyst temperatures will rise slightly. However, catalyst temperature may decrease if the reduction in gas residence time is more significant.

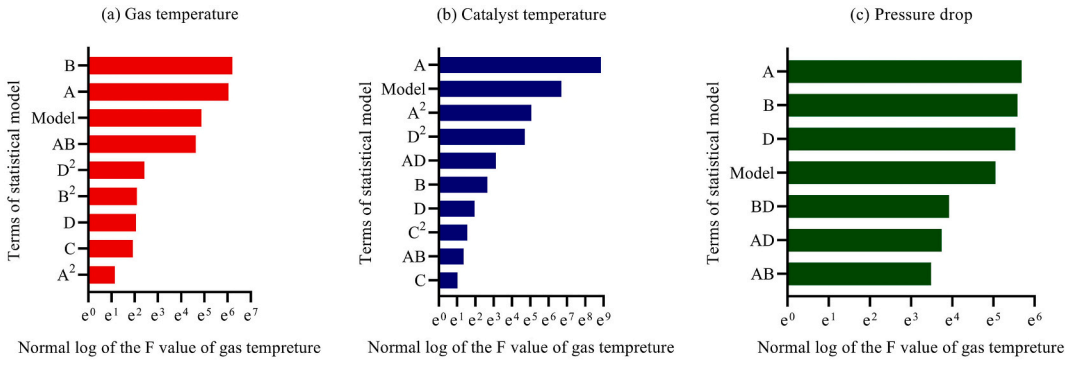

Fig. 9. Pareto plot for the relative importance of the terms of statistical models for gas temperature, catalyst temperature and pressure drop. A = Reactor outer wall temperature, B= Volumetric flowrate, C= Wall temperature time and D = Surface area of granules.

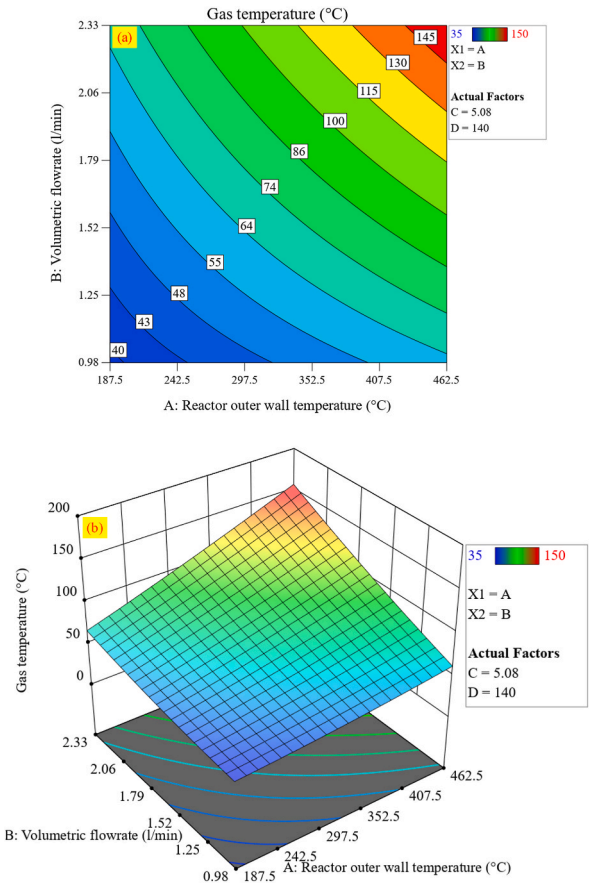

Fig. 10. 3D Response surface and contour plot of reactor outer wall temperature vs volumetric flowrate on gas temperature (°C).

Based on Fig. 13 (g and h), 14 (i and j) 15 (k and l) and Table 10, there have been significant interactions between factors of AB; p-value=<0.0001, AD; p-value=<0.0001 and BD; p-value=<0.0001 on the pressure drop. Moreover, pressure drop increased with an increase in the reactor outer wall temperature and the volumetric flow rate and surface area of granules to a certain extent. The increase in pressure drop within the preheating chamber is directly influenced by the reactor outer wall temperature, volumetric flow rate, and surface area of quartz granules due to several interrelated factors. Higher reactor wall temperatures reduce gas density and increase viscosity, leading to greater frictional resistance and higher gas velocity, both of which contribute to increased pressure drop. Additionally, gas velocity increases as the volumetric flow rate rises, which further amplifies frictional losses, particularly as the flow may transition to a more turbulent regime. Moreover, an increase in the surface area of the granules enhances contact between the gas and solid surfaces, increasing friction and narrowing the flow pathways, thereby further raising the pressure drop [68]. These combined effects result in a significant increase in pressure drop under the given conditions.

3.5.1. Optimization

Our goal is to optimize the parameters to achieve the highest thermal efficiency of the reactor and the lowest pressure drop and the cost implications. This involves considering the responses of pressure drop and the ratios of gas and catalyst temperature, and pressure drop to the reactor outer wall temperature. The purpose of this optimization is to achieve the highest indexes of "gas temperature/reactor outer wall temperature" and "catalyst temperature/reactor outer wall temperature" and to achieve the lowest wall temperature time, pressure drop, and the index of "pressure drop/reactor outer wall temperature" in the preheating chamber. The predicted responses of the optimum conditions were obtained using the point prediction. Table 12 provides information on the examined parameters, their respective importance, and the favorable changes in responses as determined by the researchers of the present study. The related indicators (GT/ROWT, CT/ROWT, and PD/ROWT) were used here since gas and catalyst temperature do not directly influence the optimization process.

As can be seen in Table 12, the numerical optimization was carried out by keeping the parameters of A, B, and D in the range (between $\pm\alpha$) and maximizing the ratio of gas temperature to reactor outer wall temperature and also the ratio of catalyst temperature to reactor outer wall temperature, and minimizing the wall temperature time, pressure drop and the ratio of pressure drop to reactor outer wall temperature, which was found to vary from 0.095 to 0.62, 0.966 to 1.236, 0.16–10 min, 7–153 Pa, 0.021 to 0.33 $Pa/^{\circ}C$, respectively. Various degrees of importance were assigned to these parameters. Since the investigated catalyst is of a thermal type and

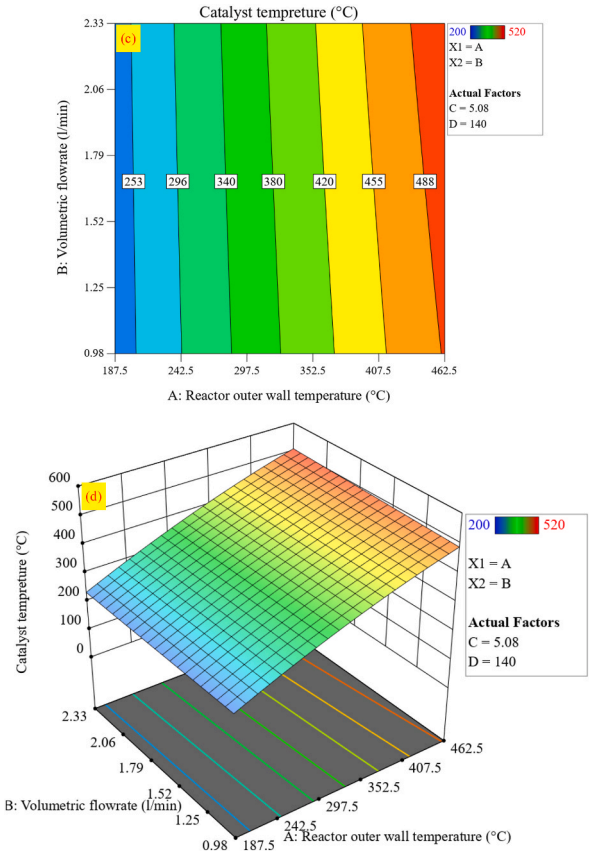

Fig. 11. 3D Response surface and contour plot of reactor outer wall temperature vs volumetric flowrate on catalyst temperature (°C).

gas and catalyst temperatures play a crucial role in pollutant removal efficiency, temperature responses were prioritized over pressure drop in this optimization.

The solution and validation of the optimized response are shown in Table 13. It presents the predicted optimal levels (P values) of the main design-operational variables required to achieve an acceptable level of the studied responses in the quartz reactor with a preheating chamber based on the goals and importance defined in Table 12. To confirm these results, the reactor factors were then carried out at those optimum conditions and were analyzed for the performance of the reactor, i.e., actual responses (A values). It was found that the actual values of the responses (A) obtained were well represented by the values (P) predicted by the model Equations (14)–(16). It should be noted that optimal conditions are achieved when the outer wall temperature, the flow rate, the wall temperature time, and the granules' surface area are 230 Ċ, 3 L/min, 0.16 min, and 67.3 cm^2, respectively.

According to JORGE et al. [24], a comprehensive understanding of these reactors necessitates grasping three crucial thermal transfer terms: heat transfer from the furnace chamber to the reactor wall (predominantly radiation), within the wall (conduction), and from the wall to the catalytic fixed bed. This understanding is visually represented in Fig. 16, where the total heat-transfer resistance (Req) is depicted as a combination of three thermal resistances in series: the resistance in the furnace chamber (Rext), the reactor wall resistance (Rk), and the fixed bed resistance (Rint). Equations (17)–(20) can calculate these thermal resistances.

$$R_{int} = \frac{1}{U_{int} A_i} \tag{17}$$

$$R_k = \frac{(r_e - r_i) + L_{AC}}{k A_{lm}} \tag{18}$$

$$R_{ext} = \frac{1}{h_{ext} A_e} \tag{19}$$

Combining these resistances leads to:

$$R_{eq} = \frac{1}{U_{eq} A_i} = \frac{1}{h_{ext} A_e} + \frac{r_e - r_i}{k A_{lm}} + \frac{1}{U_{int} A_i} \tag{20}$$

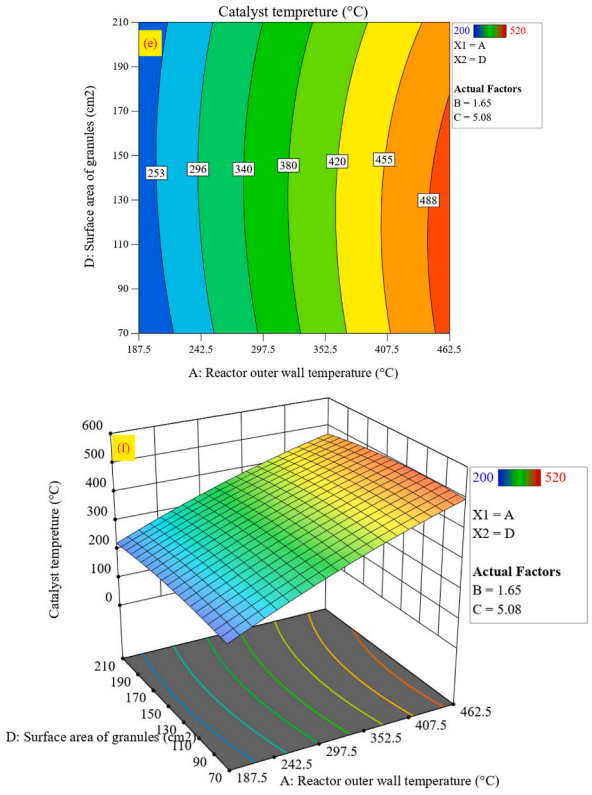

Fig. 12. 3D Response surface and contour plot of reactor outer wall temperature vs surface area of granules on catalyst temperature (°C).

The internal (subscript i) and external (subscript e) radius and area of the reactor tube are represented by r and A. Alm denotes the logarithmic mean area.

The physical characteristics of quartz granules in preheating chamber, including diameter (2.4 ± 0.01 mm), weight (0.017 ± 0.002 gr), surface area (18.22 ± 2.17 mm^2), volume (7.27 ± 1.29 mm^3), volume density (2.34 ± 0.1 gr/cm^3) and surface density (0.09 ± 0.005 gr/cm^2) have been depicted in Table 1.

WELLAUER and CRESSWEL [69] investigated the effects of tube diameter, coolant temperature, air mass velocity, packing size, shape, and thermal conductivity on the overall heat transfer coefficient. The results showed that particle conductivity and tube diameter, within their range of variation, have only marginal effects on the overall heat transfer coefficient. Moreover, not only was mass velocity an essential effect on the overall heat transfer coefficient, but particle shape was also important.

It is believed that the increase in voids with an increase in the size of the particles is caused by the relative smallness of the container. The container wall prevents the spheres from settling into their normal positions in the bed. Larger particles experience a more pronounced effect. In large containers, in which the wall effect is negligible, the voids in the bed are independent of the size of the particle [70]. That those factors which increase resistance to fluid flow also increase the coefficient of heat transfer is a reasonable hypothesis. With dimensional analysis, this assumption agrees with experimental facts [71]. Moreover, the small particles seem to have a proportionately more “dead” area-where the gas stream does not strike the surface [70].

The heat transfer rate in a packed bed is essential for the process design of heat exchangers and catalytic reactors. Researchers have studied the issue of heat transfer rate from tube walls to fluid in packed tubes. Colburn [72] was the first to investigate heat transfer in a packed bed. The Pareto plot in Fig. 9 illustrates the relative significance of statistical model terms for gas temperature, catalyst temperature, and pressure drop. As can be seen, the reactor outer wall temperature is an influential factor that results in a decrease in the ratio of GT/ROWT at low to moderate temperature range and a slight increase of this index at high temperatures. It is essential to mention that as the temperature rises, thermal conductivity, specific heat, and linear velocity increase under a constant gas flow rate. All these changes tend to increase the coefficient of heat transfer. On the flip side, the gas becomes more viscous when the temperature increases, decreasing heat transfer [70]. Therefore, despite the dominance of the viscosity factor at lower ROWT, the first three changes have had a more significant effect than the last one at higher ROWT.

Colburn [72] meticulously examined the influence of the mass velocity of the gas and the ratio of particle diameter to container diameter on the heat transfer coefficient. Experimental results revealed that heat transfer coefficients to the air flowing through a tube filled with granular materials are approximately eight times higher than expected for the same gas rate through an empty tube. This finding aligns perfectly with our present data. Our study also found that increasing the volumetric flow rate significantly impacts gas temperature, raising it while slightly decreasing the temperature at the center of the catalyst, particularly at higher reactor wall

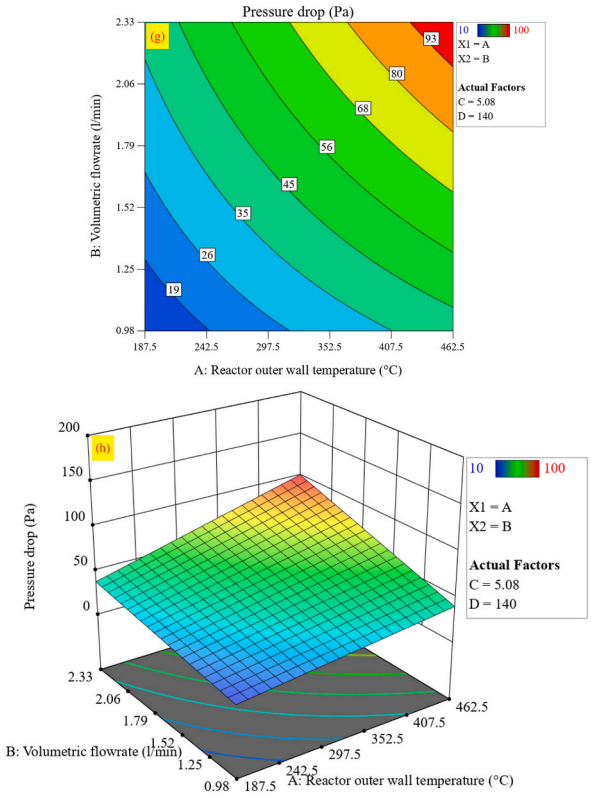

Fig. 13. 3D Response surface and contour plot of reactor outer wall temperature vs volumetric flowrate on pressure drop (Pa).

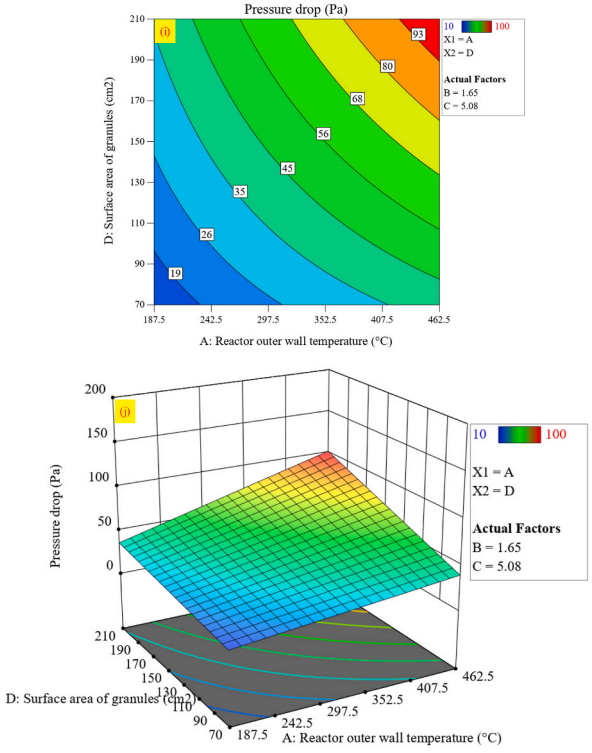

Fig. 14. 3D Response surface and contour plot of reactor outer wall temperature vs surface area of granules on pressure drop (Pa).

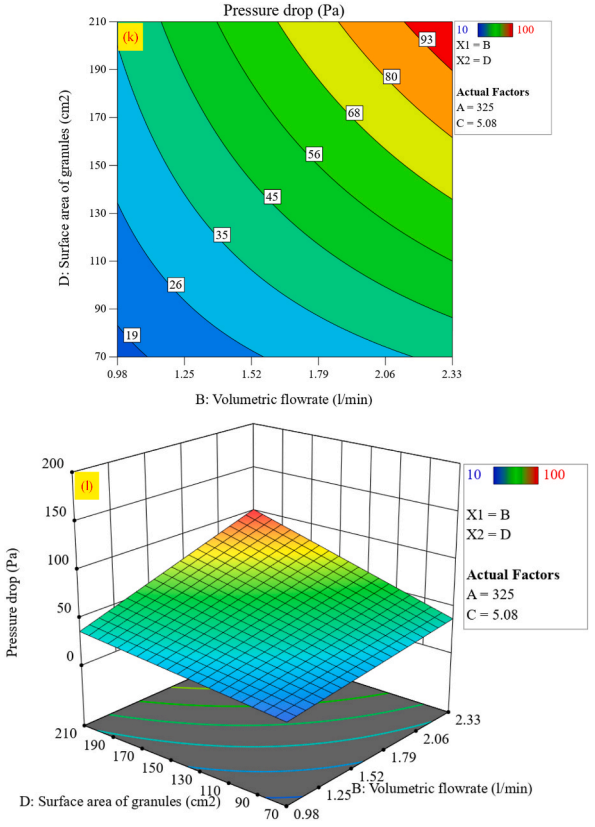

Fig. 15. 3D Response surface and contour plot of volumetric flowrate vs surface area of granules on pressure drop (Pa).

Table 12
Variables, their respective importance and the favorable changes of responses.

Name	Goal	Lower Limit	Upper Limit	Lower Weight	Upper Weight	Importance
A:Reactor outer wall temperature (Ċ)	is in range	50	600	1	1	3
B:Volumetric flowrate (L/min)	is in range	0.3	3	1	1	3
C:Wall temperature time (min)	minimize	0.16	10	1	1	2
D:Surface area of granules (cm^2)	is in range	0	210	1	1	3
Gas temperature (Ċ)	none	–	–	–	–	–
Catalyst temperature (Ċ)	none	–	–	–	–	–
Pressure drop (Pa)	minimize	7	153	1	1	2
Gas temperature/Reactor outer wall temperature	maximize	0.0953846	0.62	1	1	5
Catalyst temperature/Reactor outer wall temperature	maximize	0.966486	1.236	1	1	5
Pressure drop/Reactor outer wall temperature (Pa/ Ċ)	minimize	0.0215385	0.33	1	1	3

Table 13
Optimal conditions of variables for quartz reactor equipped with preheating chamber.

Variables				Responses											
ROWT (Ċ)	VF (L/min)	WTT (min)	SAG (cm^2)	GT (Ċ)		CT (Ċ)		PD (Pa)		GT/ROWT		CT/ROWT		PD/ROWT (Pa/Ċ)	
				P	A	P	A	P	A	P	A	P	A	P	A
230	3	0.16	67.3	103	105.3	267	264.6	25	25.3	0.475	0.457	1.158	1.15	0.14	0.109

ROWT: Reactor outer wall temperature. VF: Volumetric flowrate. WTT: Wall temperature time. SAG: Surface area of granules. GT: Gas temperature. CT: Catalyst temperature. PD: Pressure drop. GT/ROWT: Gas temperature/Reactor outer wall temperature. CT/ROWT: Catalyst temperature/Reactor outer wall temperature. PD/ROWT: Pressure drop/Reactor outer wall temperature. P: Predicted. A: Actual.

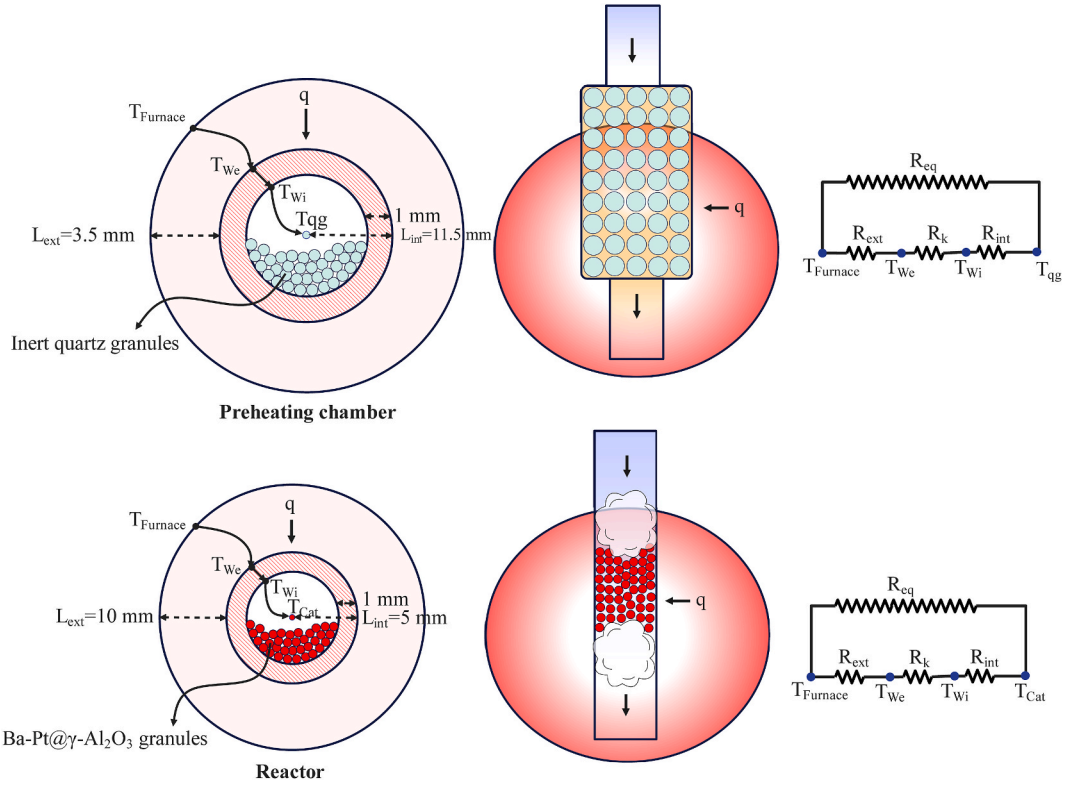

Fig. 16. Radial heat flow through the reactor and preheating chamber.

temperatures.

Furthermore, according to Furnas [70], the coefficient of heat transfer increases with higher gas velocity, likely due to the reduction in thickness of the stagnant gas film around the particles. This film primarily hinders heat transfer; therefore, decreasing its thickness may increase heat transfer. Moreover, the research by Mansoorzadeh et al. is of significant importance. Their simulation of fixed beds using the 3D finite element method revealed that increasing the drag coefficient at high Reynolds and reducing the space between the spheres can notably enhance the heat transfer from the spheres [73]. Similarly, the work of Eslami et al. is crucial. They demonstrated that flow channelization, which intensifies with the increase in flow rate, occurs near the wall and inside the bed. This phenomenon leads to a rise in axial flows and a decline in radial flows, ultimately reducing the convection heat transfer rate [74]. In addition, Colburn [72] underscores the practical implications of his research, noting that the absence of uniform packing next to the tube wall causes less resistance to gas flow, resulting in a higher velocity in this region compared to the center of the packing. He suggests that the cross-sectional area affected by the wall is determined by the perimeter of the pipe and the diameter of the particles and is proportional to $D \times D_t$. Equation (21) can calculate the approximate ratio between this area and the remaining cross-sectional area.

$$\frac{D \times \pi D_t}{\frac{\pi}{4} \times D_t^2} = 4\, D/D_t \tag{21}$$

Consequently, when the ratio of D/D_t increases, a higher proportion of the gas will flow adjacent to the wall, increasing heat transfer. When the ratio of D/D_t exceeds 0.15, the particles in the center of the tube do not pack closely together. This causes larger spaces, decreased flow near the wall, and lower heat-transfer coefficients.

In addition, Chilton and Colburn [75] present a general method of predicting pressure drops in both the viscous and turbulent regions. It has been demonstrated that a substantial part of the pressure drop is caused by expansion and contraction losses. Zeisberg [76] was the first to significantly research tower packing's pressure drop. His findings showed that the pressure drop is directly proportional to the square of the linear gas velocity.

The optimization process for the quartz reactor with a preheating chamber, as detailed in the provided data, reveals several key insights relevant to industrial applications, cost implications, and scalability.

For potential industrial applications, the optimized conditions, particularly the reactor outer wall temperature (ROWT) of 230 °C, a high volumetric flowrate (VF) of 3 L/min, and minimal wall temperature time (WTT) of 0.16 min, demonstrate the high efficiency of this configuration for processes requiring rapid gas heating, effective catalyst activation and specially catalyst studies. These conditions are especially beneficial in industries such as petrochemical refining and catalytic conversion processes, where precise control over gas and catalyst temperatures is crucial. The moderate surface area of granules (SAG) at 67.3 cm^2 supports efficient heat transfer without causing excessive pressure drop, making this setup suitable for large-scale operations. Moreover, the optimized reactor

conditions, particularly the minimal wall temperature time (WTT) of 0.16 min, offer significant cost advantages by reducing the energy required to maintain the reactor at the desired operational temperatures. This brief heating period before testing is sufficient to achieve the highest gas temperature to reactor wall temperature ratio and the highest catalyst temperature to reactor wall temperature ratio, all while minimizing the pressure drop and the pressure drop to reactor wall temperature ratio. These optimized ratios indicate that the reactor operates more efficiently, transferring heat effectively to the gas and catalyst without unnecessary energy expenditure. Energy consumption is reduced by minimizing the time the reactor needs to be maintained at high temperatures before testing, leading to lower operational costs. The combined effect of efficient heat transfer and reduced pressure drop ensures that the reactor operates at optimal conditions with minimized energy input, directly leading to lower overall costs and improved economic viability in industrial applications.

It should be noted that scalability refers to the ability of the reactor system to be expanded or adjusted to accommodate larger production scales or higher operational demands while maintaining efficiency and performance. While some aspects of the reactor design and its operation may exhibit linear relationships, making it easier to predict and manage changes when scaling up, it is essential to note that not all relationships are linear. The presence of non-linear interactions between factors—such as the reactor outer wall temperature, volumetric flow rate, and surface area of granules—can introduce complexities when scaling up. Non-linearities in the system mean that specific parameters may not simply double their effect when scaled up; their impact might grow disproportionately. For example, increases in flow rate or surface area might lead to unexpected changes in pressure drop or heat transfer efficiency, requiring careful re-optimization of the process at larger scales. Therefore, while scalability is feasible, careful consideration of these non-linear relationships is required, and adjustments to the design and operational parameters may be necessary to ensure that the reactor performs optimally under new conditions.

While the optimization results are promising, the study has inherent limitations that should be acknowledged. The study focuses on a specific range of temperatures, flow rates, wall temperature time, and granule surface areas. Expanding the experimental scope to include a broader range of conditions, particularly at extreme ends, would provide a more comprehensive understanding of the reactor's behavior and applicability in different laboratory and industrial scenarios. In addition, the long-term stability of the optimized conditions, particularly under continuous operation, has not been fully explored. Future studies should investigate the potential for fouling, wear, and other degradation mechanisms that could affect the reactor's performance over time.

Further research could explore the detailed thermodynamics and reaction kinetics within the preheating chamber and the catalyst bed. This would help refine the model and identify new optimization strategies that could further enhance the reactor's efficiency and reduce operational costs. Moreover, exploring the application of this optimized reactor design with different types of catalysts or catalytic reactions could provide valuable insights into its versatility and adaptability to various chemical processes.

4. Conclusion

The motivation arises from an ongoing study on NOx removal efficiency by NSR catalyst, where adequate supply and control of heat to the gas temperature and packed bed are crucial. This study presents a comprehensive analysis and optimization of a lab-scale quartz reactor with a preheating chamber, focusing on the critical parameters influencing gas and catalyst temperatures, and pressure drop. The optimized values of the reactor outer wall temperature, volumetric flow rate, wall temperature time, and surface area of granules for maximizing the ratio of gas temperature to reactor outer wall temperature (GT/ROWT) and also the ratio of catalyst temperature to reactor outer wall temperature (CT/ROWT), and minimizing the wall temperature time (WTT), pressure drop and the ratio of pressure drop to reactor outer wall temperature (PD/ROWT) were determined using the RSM, following the CCD. The optimal conditions were a reactor outer wall temperature of 230 Ċ, a volumetric flow rate of 3 L/min, a wall temperature time of 0.16 min, and a surface area of granules of 67.3 cm^2. Experimental results under these optimal conditions yielded a gas temperature of 105.3 °C, a catalyst temperature of 264.6 °C, GT/ROWT of 0.457, CT/ROWT of 1.15, a pressure drop of 25.3 Pa, and PD/ROWT of 0.109. These results closely aligned with the predicted values, demonstrating the accuracy and effectiveness of the optimization process. By reducing pressure drop and improving heat transfer efficiency, the study provides valuable insights for the design and operation of catalytic reactors, particularly in applications where heat management is critical, such as thermal catalysts.

Funding

This study was part of a PhD thesis and was financially supported by Tarbiat Modares University (Med90278).

Ethical statement

This study was reviewed and approved by the ethics committee of Tarbiat Modares University with the approval number: IR.MODARES.REC.1400.309, dated January 26, 2022.

Consent for publication

All authors performed editing and approving the final version of this paper for submission, also participated in the finalization of the manuscript and approved the final draft.

Data availability statement

The data that support the findings of this study are available from Dr. Javad Sajedifar but restrictions apply to the availability of these data, which were used under license for the current study, and so are not publicly available. Data are however available from the authors upon reasonable request and with permission of Dr. Javad Sajedifar.

CRediT authorship contribution statement

Javad Sajedifar: Writing – review & editing, Writing – original draft, Software, Investigation, Formal analysis, Data curation. **Seyyed Bagher Mortazavi:** Writing – review & editing, Writing – original draft, Supervision, Conceptualization. **Hasan Asilian Mahabadi:** Writing – review & editing, Writing – original draft, Project administration, Methodology.

Declaration of competing interest

The authors declare that they have no known competing financial interests or personal relationships that could have appeared to influence the work reported in this paper.

Acknowledgments

The authors appreciate the authorities of the University for their financial support. The authors would like to express their appreciation to Dr. Ali Khavanin, Dr. Mohammad-Sharif Hoseini, Dr. Gholamreza Moussavi, and Dr. Ali Morsali at Tarbiat Modares University for providing Some laboratory equipment needed and for their sincere cooperation.

Abbreviations

GDI	Gasoline Direct Injection
TWC	Three-Way Catalysts
LNT	Lean NOx Trap
NSR	NOx Storage Reduction
SCR	Selective Catalytic Reduction
ID	Internal Diameter
ED	External Diameter
RSM	Response Surface Methodology
NSR	NOx Storage Reduction
CCD	Central Composite Design
CV	Coefficient of Variation
2FI	2 Factor Interaction
ANOVA	Analysis Of Variance
$\mathbf{R^2}$	Determination of coefficient
$\mathbf{R^2_{adj}}$	Adjusted coefficient of determination
SSQ	Sum Of Squares
$\mathbf{SSQ_{mod}}$	Sum Of Squares of model
$\mathbf{SSQ_{residual}}$	Sum Of Squares of residual
$\mathbf{DgF_{mod}}$	Degree of Freedom of model
$\mathbf{DgF_{residual}}$	Degree of Freedom of residual
LT	Low temperature
HT	High temperature
CV	Coefficient of Variation
F-value	Model significance
SD	Standard Deviation
MnS_{RD}	Mean of square residual
MnS_{RG}	Mean of square regression
eq	equivalent, overall
int	internal
ext	external
k	relative to wall conduction
A	heat-transfer area (m^2)
h	heat-transfer coefficient ($W/m^2/°C$)
k	conductivity ($W/m/°C$)
R	thermal resistance ($°C/W$)
r	tube radius (m)

T	temperature (°C)
U	heat-transfer coefficient (W/m^2/°C)
w	wall
D_t	tube diameter (m)
T_{qg}	**temperature of quartz granules in preheating chamber**

Appendix A. Supplementary data

Supplementary data to this article can be found online at https://doi.org/10.1016/j.heliyon.2024.e38087.

References

[1] H.-S. Kim, et al., Current catalyst technology of selective catalytic reduction (SCR) for NOx removal in South Korea, Catalysts 10 (1) (2020) 52.
[2] S. Roy, A. Baiker, NO x storage− reduction catalysis: from mechanism and materials properties to storage− reduction performance, Chem. Rev. 109 (9) (2009) 4054–4091.
[3] M. Daturi, et al., Room temperature reduction of nitrogen oxide on iron metal-organic frameworks, Adv. Mater. (2023) 2403053.
[4] P.G. Smirniotis, D.A. Peña, B.S. Uphade, Low-temperature selective catalytic reduction (SCR) of NO with NH 3 by using Mn, Cr, and Cu oxides supported on hombikat TiO 2, Angew. Chem. 40 (13) (2001) 2479–2482.
[5] J.H. Seinfeld, S.N. Pandis, Atmospheric Chemistry and Physics: from Air Pollution to Climate Change, John Wiley & Sons, 2016.
[6] B.J. Finlayson-Pitts, J.N. Pitts Jr., Chemistry of the Upper and Lower Atmosphere: Theory, Experiments, and Applications, Elsevier, 1999.
[7] D.J. Jacob, Introduction to atmospheric chemistry (1999).
[8] R. Aghababaei-Talkhonche, et al., Catalytic removal of NO2 by nickel–platinum catalyst supported on multi-wall carbon nanotubes, Global Nest Journal 22 (2) (2020) 231–239.
[9] K. Wark, C. Warner, W. Davis, Air pollution: its Origin and Control, 3. Baskı, Addison-Wesley Longman, Inc., ABD, 1998.
[10] N.W. Cant, M.J. Patterson, The storage of nitrogen oxides on alumina-supported barium oxide, Catal. Today 73 (3–4) (2002) 271–278.
[11] W. Bögner, et al., Removal of nitrogen oxides from the exhaust of a lean-tune gasoline engine, Appl. Catal. B Environ. 7 (1–2) (1995) 153–171.
[12] W.S. Epling, et al., Overview of the fundamental reactions and degradation mechanisms of NOx storage/reduction catalysts, Catal. Rev. 46 (2) (2004) 163–245.
[13] D. Tomazic, M. Tatur, M. Thornton, Development of a diesel passenger car meeting tier 2 emissions levels, SAE Trans. (2004) 300–315.
[14] K. Nakatani, et al., Simultaneous PM and NOx reduction system for diesel engines, SAE Trans. (2002) 362–369.
[15] L. Xu, G. Graham, R. McCabe, A NO x trap for low-temperature lean-burn-engine applications, Catal. Lett. 115 (2007) 108–113.
[16] N. Miyoshi, S.i. Mastumoto, NOx Storage-reduction catalyst (nsr catalyst) for automotive engines: sulfur poisoning mechanism and improvement of catalyst performance, in: H. Hattori, K. Otsuka (Eds.), Studies in Surface Science and Catalysis, Elsevier, 1999, pp. 245–250.
[17] S.i. Matsumoto, Recent advances in automobile exhaust catalysts, Catal. Today 90 (3) (2004) 183–190.
[18] R. Bonzi, et al., NOx removal over a double-bed NSR-SCR reactor configuration, Catal. Today 151 (3) (2010) 376–385.
[19] C. Lijuan, et al., Influence of CO2 concentration and inlet temperature on adsorption path of lean NOx Trap, Energy Proc. 158 (2019) 4383–4388.
[20] A.G. Dixon, B. Partopour, Computational fluid dynamics for fixed bed reactor design, Annu. Rev. Chem. Biomol. Eng. 11 (2020) 109–130.
[21] J. Worstell, Chapter 5 - scaling fixed-bed reactors, in: J. Worstell (Ed.), Adiabatic Fixed-Bed Reactors, Butterworth-Heinemann, Boston, 2014, pp. 81–108.
[22] D. Marin, et al., Design and validation study of a laboratory scale chemical reactor for non-invasive imaging of macro objects in situ, Chem. Eng. J. 327 (2017) 889–897.
[23] J. Hua, M. Wu, K. Kumar, Numerical simulation of the combustion of hydrogen–air mixture in micro-scaled chambers. Part I: fundamental study, Chem. Eng. Sci. 60 (13) (2005) 3497–3506.
[24] L.M.d.M. Jorge, et al., Evaluation of heat transfer in a catalytic fixed bed reactor at high temperatures, Braz. J. Chem. Eng. 16 (1999) 407–420.
[25] F. Augier, F. Idoux, J.-Y. Delenne, Numerical simulations of transfer and transport properties inside packed beds of spherical particles, Chem. Eng. Sci. 65 (3) (2010) 1055–1064.
[26] J. Yang, et al., Computational study of fluid flow and heat transfer in composite packed beds of spheres with low tube to particle diameter ratio, Nucl. Eng. Des. 300 (2016) 85–96.
[27] M. Zhang, H. Dong, Z. Geng, Computational study of flow and heat transfer in fixed beds with cylindrical particles for low tube to particle diameter ratios, Chem. Eng. Res. Des. 132 (2018) 149–161.
[28] T.D. Vavanellos, Design Of A Simple Apparatus For Reaction Kinetics And Reactor Design Experiments (1990).
[29] J.J. Carberry, Designing laboratory catalytic reactors, Ind. Eng. Chem. 56 (11) (1964) 39–46.
[30] N. Yaghobi, The role of gas hourly space velocity and feed composition for catalytic oxidative coupling of methane: experimental study, Journal of King Saud University-Engineering Sciences 25 (1) (2013) 1–10.
[31] R. Aghababaei Talkhonche, et al., NO2 catalytic removal by nickel catalyst supported on multi-walled carbon nanotubes, Int. J. Environ. Stud. 78 (3) (2021) 427–443.
[32] Y.M. Morteza Saedi Marghmaleki Ak, Investigation on the Effect of Plasma-Nanocatalyst System to Reduce Emissions of Gasoline Engines, University of Tehran, 2017.
[33] S. Athar, H. Asilian, Catalytic oxidation of carbon monoxide using copper-zinc mixed oxide nanoparticles supported on diatomite, Health Scope 1 (2) (2012).
[34] Y. Chu, J.A. Storrow, Heat transfer to air flowing through packed tubes, Chem. Eng. Sci. 1 (5) (1952) 230–237.
[35] X. Xu, et al., Ordered mesoporous alumina and their composites based on evaporation induced self-assembly for adsorption and catalysis, Chem. Mater. 32 (1) (2019) 3–26.
[36] L. Lietti, et al., NOx storage reduction over Pt Ba/γ-Al2O3 catalyst, J. Catal. 204 (1) (2001) 175–191.
[37] F. Frola, et al., Combined in situ FT-IR and TRM analysis of the NOx storage properties of Pt-Ba/Al2O3 LNT catalysts, Catal. Today 126 (1–2) (2007) 81–89.
[38] H. Shinjoh, N. Takahashi, K. Yokota, Synergic effect of Pd/γ-alumina and Cu/ZSM-5 on the performance of NO x storage reduction catalyst, Top. Catal. (2007).
[39] N. Miyoshi, et al., European Patent Application EP 0 669 (157) (1995) A1. *Paper 950809 (1995)*.
[40] T. Senthilkumar, S. Chattopadhyay, L.R. Miranda, Optimization of activated carbon preparation from pomegranate peel (Punica granatum peel) using RSM, Chem. Eng. Commun. 204 (2) (2017) 238–248.
[41] M.A. Bezerra, et al., Response surface methodology (RSM) as a tool for optimization in analytical chemistry, Talanta 76 (5) (2008) 965–977.
[42] P. Kočí, et al., Global kinetic model for the regeneration of NOx storage catalyst with CO, H2 and C3H6 in the presence of CO2 and H2O, Catal. Today 147 (2009) S257–S264.
[43] Y. Liu, et al., Enhanced activity of CuO/K 2 CO 3/MgAl 2 O 4 catalyst for lean NO x storage and reduction at high temperatures, RSC Adv. 7 (44) (2017) 27405–27414.
[44] X. Fan, et al., Numerical investigation of boundary layer flow and wall heat transfer in a gasoline direct-injection engine, Int. J. Heat Mass Tran. 120 (2018) 1189–1199.

[45] N. Takahashi, et al., The low-temperature performance of NOx storage and reduction catalyst, Appl. Catal. B Environ. 70 (1–4) (2007) 198–204.
[46] T. Stoll, et al., A model approach to simulate exhaust gas temperatures of diesel oxidation catalysts, in: 22. Internationales Stuttgarter Symposium: Automobil-Und Motorentechnik, Springer, 2022.
[47] D.T. Koch, et al., H2-deNOx catalyst for H2 combustion engines, MTZ worldwide 81 (6) (2020) 30–35.
[48] S. Ascaso, et al., *Influence of gas hourly space velocity on the activity of monolithic catalysts for the simultaneous removal of soot and NO x.* Comptes Rendus, Chimie 18 (10) (2015) 1007–1012.
[49] S. Nassos, et al., The influence of Ni load and support material on catalysts for the selective catalytic oxidation of ammonia in gasified biomass, Appl. Catal. B Environ. 74 (1–2) (2007) 92–102.
[50] W. Shan, et al., An environmentally-benign CeO2-TiO2 catalyst for the selective catalytic reduction of NOx with NH3 in simulated diesel exhaust, Catal. Today 184 (1) (2012) 160–165.
[51] W. Wanchan, P. Khongprom, S. Limtrakul, Study of wall-to-bed heat transfer in circulating fluidized bed riser based on CFD simulation, Chem. Eng. Res. Des. 156 (2020) 442–455.
[52] R. Moradirad, et al., Investigating the factors affecting the optimization of hydrogen sulfide gas adsorption parameters on the new MIPs@H2S nanoadsorbent using the response surface method, Int. J. Environ. Sci. Technol. (2024).
[53] L. Sheriff, et al., in: Response Surface Methodology, K. Palanikumar (Eds.), Applications of Response Surface Methodology (RSM) in Product Design, Development, and Process Optimization, IntechOpen, Rijeka, 2022. Ch. 3.
[54] r. asadi, j. towfighi, s.m. mousavi, Statistical modeling and optimization of propane oxidative dehydrogenation process using gamma alumina based on molybdenum catalyst, Journal of Applied Research of Chemical -Polymer Engineering 2 (3) (2019) 21–39.
[55] M. Piacentini, M. Maciejewski, A. Baiker, Pt-Ba/alumina NOx storage-reduction catalysts: effect of Ba-loading on build-up, stability and reactivity of Ba-containing phases, Appl. Catal. B Environ. 59 (3–4) (2005) 187–195.
[56] L.M.C. Schholz, NOx Storage and Reduction over Alean-Burn Automotive Catalyst, Eindhoven University, Eindhoven, 2007.
[57] J.A. Cornell, Response Surfaces: Designs and Analyses, Marcel Dekker, Inc, 1987.
[58] G. Chen, et al., Application of response surface methodology for optimization of the synthesis of synthetic rutile from titania slag, Appl. Surf. Sci. 258 (7) (2012) 3068–3073.
[59] A. Ayeni, et al., Hydrogen peroxide and lime based oxidative pretreatment of wood waste to enhance enzymatic hydrolysis for a biorefinery: process parameters optimization using response surface methodology, Fuel 106 (2013) 187–194.
[60] S. Chatterjee, et al., Application of response surface methodology for methylene blue dye removal from aqueous solution using low cost adsorbent, Chem. Eng. J. 181 (2012) 289–299.
[61] R. Kumar, et al., Effect of process variables on the exothermicity during the production of phenol–formaldehyde resins–modeling by response surface methodology, Eur. Polym. J. 36 (11) (2000) 2491–2497.
[62] D. Dora, Y. Mohanty, G. Roy, Hydrodynamics of three-phase fluidization of a homogeneous ternary mixture of regular particles—experimental and statistical analysis, Powder Technol. 237 (2013) 594–601.
[63] K. Ravikumar, et al., Optimization of batch process parameters using response surface methodology for dye removal by a novel adsorbent, Chem. Eng. J. 105 (3) (2005) 131–138.
[64] C. Nieto-Delgado, J.R. Rangel-Mendez, Production of activated carbon from organic by-products from the alcoholic beverage industry: surface area and hardness optimization by using the response surface methodology, Ind. Crop. Prod. 34 (3) (2011) 1528–1537.
[65] J. Sajedifar, et al., The comparative assessment of welders' exposure to welding fumes based on mass and number concentration, Journal of Health & Safety at Work 6 (4) (2017).
[66] J. Sajedifar, et al., Evaluation of operational parameters role on the emission of fumes, Ind. Health 56 (3) (2018) 198–206.
[67] R.L. Mason, R.F. Gunst, J.L. Hess, Statistical Design and Analysis of Experiments: with Applications to Engineering and Science, John Wiley & Sons, 2003.
[68] S. Ahmadi, F. Sefidvash, Study of pressure drop in fixed bed reactor using a computational fluid dynamics (CFD) code, ChemEngineering 2 (2) (2018) 14.
[69] T. Wellauer, D. Cresswell, E. Newson, Heat Transfer in Packed Reactor Tubes Suitable for Selective Oxidation, ACS Publications, 1982.
[70] C.G. Furnas, Heat transfer from a gas stream to bed of broken solids, Ind. Eng. Chem. 22 (1) (1930) 26–31.
[71] W.H. McAdams, T.H. Frost, Heat transfer by conduction and convection II- liquids FLowing through pipes, J. Ind. Eng. Chem. 14 (12) (1922) 1101–1104.
[72] A.P. Colburn, Heat transfer and pressure drop in empty, baffled, and packed tubes1, Ind. Eng. Chem. 23 (8) (1931) 910–913.
[73] S. Mansoorzadeh, et al., Finite element simulations of incompressible flow past a heated/cooled sphere, Int. J. Numer. Methods Fluid. 28 (6) (1998) 903–915.
[74] E.K. Homa Eslami, Farhad Shahraki, Investigating pressure drop and heat transfer in fixed bed reactors using computational fluid dynamics, in: International Conference of Oil, Gas, Petrochemical and Power Plant, 2012.
[75] T.H. Chilton, A.P. Colburn, II—pressure drop in packed Tubes1, Ind. Eng. Chem. 23 (8) (1931) 913–919.
[76] F.C. Zeisberg, Resistance of absorption tower packing to gas flow, Chem. Met. Eng 21 (1919) 765–767.